Construction and Building Materials 353 (2022) 129161

Contents lists available at ScienceDirect

Construction and Building Materials

journal homepage: www.elsevier.com/locate/conbuildmat

Experimental assessment and constitutive modelling of rubberised One-Part Alkali-Activated concrete

M. Elzeadani [a], D.V. Bompa [a,b,*], A.Y. Elghazouli [a]

[a] Department of Civil and Environmental Engineering, Imperial College London, UK
[b] Department of Civil and Environmental Engineering, University of Surrey, UK

ARTICLE INFO

Keywords:
Rubberised concrete
Alkali-activated concrete
Crumb rubber
Blast furnace slag
Fly ash

ABSTRACT

This study deals with the development and assessment of rubberised one-part alkali-activated concrete. An experimental programme, focusing on optimising the material proportions for high flowability and compressive strength, is firstly described. This includes varying the proportions of aluminosilicate precursors, binder-to-aggregate ratio, activator dosage, and admixture quantity to find an optimum mix design with stable strength development up to 90 days. Crumb rubber particles are then added to replace up to 60 % by volume of the natural mineral aggregates. The effect of rubber addition on the mechanical properties is quantified and analytical expressions for the compressive strength, elastic modulus, splitting tensile strength, and flexural strength are presented. A database consisting of 241 conventional rubberised concrete as well as 57 rubberised alkali-activated mixes, available in the literature, is then assembled and used for direct comparison of the characteristics of different rubberised concrete materials. It is shown that the degradation in compressive strength for one-part rubberised alkali-activated concrete with high rubber replacement ratios falls within similar ranges as conventional and two-part alkali-activated rubberised concrete. However, the results show that the elastic modulus of one-part rubberised alkali-activated concrete is significantly lower than that of rubberised concrete mixes with the same compressive strength. Moreover, while the lateral crushing strain of one-part rubberised alkali-activated concrete increases with higher rubber replacement ratios, the axial crushing strain reduces slightly. It is also shown that the post-peak stress–strain response exhibits greater softening with higher rubber ratios. Based on the findings of the study, constitutive models for representing the compressive stress–-strain response and flexural stress-crack width response are proposed. The presented expressions provide insights into the fundamental mechanical properties of rubberised one-part alkali-activated concrete, hence paving the way for their potential use in structural members, particularly those requiring higher ductility, while also offering a sustainable alternative to conventional concrete materials.

1. Introduction

Alkali-activated concrete (AAC) offers a sustainable alternative to conventional concrete and is traditionally synthesized by mixing aluminosilicate precursors with an alkaline solution [1,2]. Precursors used in AAC have chemical compositions that are rich in aluminium oxide (Al_2O_3) and silicon dioxide (SiO_2), and often calcium oxide (CaO) as well, and can be derived from natural sources (i.e., metakaolin) or industrial by-products (i.e., fly ash, blast furnace slag) [3]. Common alkaline solutions employed in AAC include sodium hydroxide/silicates and potassium hydroxide/silicates [4]. Several studies highlighted that AAC has similar mechanical properties and often superior durability to OPC-based conventional concrete material (CCM) [5–7]. Yet, the use of a caustic alkaline solution in the two-part production method has hampered the acceptance of AAC for in-situ applications [8,9]. This encouraged researchers to look at one-part 'just-add-water' alkali-activated materials (AAMs) where a solid activator is dry-mixed with the precursors and natural aggregates, and then water is added to initiate the reaction [10–12].

Previous studies on one-part AAMs experimented with various precursors including fly ash (FA) [13,14], fly ash sinking beads (FASB) [15,16], ground granulated blast furnace slag (GGBS) [11,17], lithium slag [18,19], metakaolin [20,21], red mud [22,23], and rice husk ash [24]. The majority of studies on one-part AAMs used FA or GGBS as precursors, with some using the two in combination [10,12,25], mainly

* Corresponding author at: Department of Civil and Environmental Engineering, University of Surrey, UK.
E-mail address: d.bompa@surrey.ac.uk (D.V. Bompa).

https://doi.org/10.1016/j.conbuildmat.2022.129161
Received 9 February 2022; Received in revised form 28 August 2022; Accepted 11 September 2022
0950-0618/© 2022 The Author(s). Published by Elsevier Ltd. This is an open access article under the CC BY license (http://creativecommons.org/licenses/by/4.0/).

Nomenclature

Abbreviations

AAC	Alkali-activated concrete
AAMs	Alkali-activated materials
b/agg	Binder-to-aggregate ratio
CCM	Conventional concrete material
CNA	Coarse natural aggregates
COV	Coefficient of variation
CR	Crumb rubber
C-A—S—H	Calcium-aluminum–silicate-hydrate
C—S—H	Calcium-silicate-hydrate
DIC	Digital image correlation
FA	Fly ash
FASB	Fly ash sinking beads
FNA	Fine natural aggregates
GGBS	Ground granulated blast furnace slag
ITZ	Interfacial transition zone
LOI	Loss on ignition
MP	Megapixel
NA	Natural aggregates
N-A—S—H	Sodium-aluminum–silicate-hydrate
OPC	Ordinary Portland cement
RuAAC	Rubberised alkali-activated concrete
RuC	Rubberised concrete
SEM	Scanning electron microscope
SF	Silica fume
SP	Superplasticizer
UPV	Ultrasonic pulse velocity

Chemical formulae:

Al_2O_3	Aluminum oxide
$CaCO_3$	Calcium carbonate
CaO	Calcium oxide
$Ca(OH)_2$	Calcium hydroxide
CO_2	Carbon dioxide
KOH	Potassium hydroxide
$NaAlO_2$	Sodium aluminate
NaOH	Sodium hydroxide
$Na_2B_4O_7{\cdot}10H_2O$	Sodium tetraborate decahydrate-borax
Na_2CO_3	Sodium carbonate
Na_2O	Sodium oxide
Na_2SiO_3	Sodium silicate
$Na_2SiO_3{\cdot}5H_2O$	Sodium metasilicate pentahydrate
$Na_2SiO_3{\cdot}9H_2O$	Sodium metasilicate nonahydrate
Na_2SO_4	Sodium sulphate
SiO_2	Silicon dioxide

Symbols:

d_{50}	Median particle size
E_c	Elastic modulus
E_{c0}	Elastic modulus of the reference mix with $\rho_{vr} = 0$
$E_{c\text{-}pred}$	Predicted elastic modulus
f_c	Compressive strength
f_{c0}	Compressive strength of the reference mix with $\rho_{vr} = 0$
$f_{c,cube}$	Cube compressive strength
$f_{c(d)}$	Compressive strength of concrete specimen requiring conversion
$f_{c,ref}$	Compressive strength of reference concrete specimen
$f_{c\text{-}pred}$	Predicted compressive strength
f_f	Flexural strength
f_{f0}	Flexural strength of the reference mix with $\rho_{vr} = 0$
$f_{f\text{-}pred}$	Predicted flexural strength
f_{sp}	Splitting tensile strength
f_{sp0}	Splitting tensile strength of the reference mix with $\rho_{vr} = 0$
$f_{sp\text{-}pred}$	Predicted splitting tensile strength
$g_{c,2}$,	Post-crushing energy
G_c	Compressive crushing energy
$G_{c\text{-}f}$	Energy dissipation under flexural loading
$G_{c\text{-}nor}$	Normalised crushing energy
$G_{c\text{-}sp}$	Energy dissipation under splitting tensile loading
$V_{c(d)}$	Volume of concrete specimen requiring conversion
$V_{c,ref}$	Volume of reference concrete specimen
w	Crack width
$w_{max,0}$	Ultimate crack displacement of the reference mix ($\rho_{vr} = 0$)
$w_{max,c}$	Ultimate crack displacement
ε	Strain
$\varepsilon_{c,1}$	Axial strain
$\varepsilon_{c,2}$	Lateral strain
$\varepsilon_{cr0,1}$	Axial crushing strain of the reference mix with $\rho_{vr} = 0$
$\varepsilon_{cr,1}$	Axial crushing strain
$\varepsilon_{cr,2}$	Lateral crushing strain
ρ	Density
ρ_{vr}	Volumetric rubber replacement ratio
σ	Stress
σ_f	Flexural stress
σ_{sp}	Splitting tensile stress

due to their favourable physiochemical properties. FA is a by-product of burning coal in electricity generating power stations [26,27]; while GGBS is a by-product of iron manufacturing [10,28]. GGBS has a high CaO content and its alkali-activation results in the formation calcium-aluminium–silicate-hydrate (C-A—S—H) gels [29], which are similar to the calcium-silicate-hydrate (C—S—H) gel phases that usually result from OPC hydration [29]. Meanwhile, the alkali-activation of low calcium FA (Class F) forms a three-dimensional sodium-aluminium–silicate-hydrate (*N*-A—S—H) gels [30]. The combination of GGBS and low calcium FA in AAMs results in complex hydration products that contain both C-A—S—H and *N*-A—S—H gels [29].

Several solid activators were used to synthesize one-part AAMs, including sodium hydroxide (NaOH) [31,32], potassium hydroxide (KOH) [33,34], sodium silicates (Na_2SiO_3) [16,19,32], sodium carbonate (Na_2CO_3) [35,36], sodium aluminate ($NaAlO_2$) [15,37], sodium sulphate (Na_2SO_4) [38,39], and calcium hydroxide ($Ca(OH)_2$) [40,41]. A comparative study on the use of anhydrous sodium metasilicate (Na_2SiO_3-anhydrous), NaOH powders, and KOH pellets in FA and GGBS-based one-part AAMs, concluded that around 8 % of Na_2SiO_3-anhydrous by binder mass was optimal when considering mix flow and compressive strength [33]. Na_2SiO_3-anhydrous also gave the most favourable compressive strength in FASB- and GGBS-based one-part AAMs, compared with sodium metasilicate nonahydrate ($Na_2SiO_3{\cdot}9H_2O$) and sodium metasilicate pentahydrate ($Na_2SiO_3{\cdot}5H_2O$) [42]. Meanwhile, to improve the rheology and delay the setting of one-part AAMs, various admixtures were employed. Results show that polycarboxylate-based superplasticizers (SPs), lignosulfonate-based SPs, sucrose, or sodium tetraborate decahydrate-borax can be used in FA and GGBS-based one-part AAMs [7,43–45].

Besides AAMs, rubberised concrete (RuC) provides a viable path to recycle discarded end-of-life tyres and reduce the depletion of natural aggregates (NA) [46,47]. In RuC, a proportion of the NA is replaced by small rubber particles obtained from discarded tyres. The addition of rubber causes a reduction in the mechanical properties depending on the rubber replacement ratio [48,49]. In contrast, the ductility and energy dissipation improve with higher rubber replacement of NA [50,51].

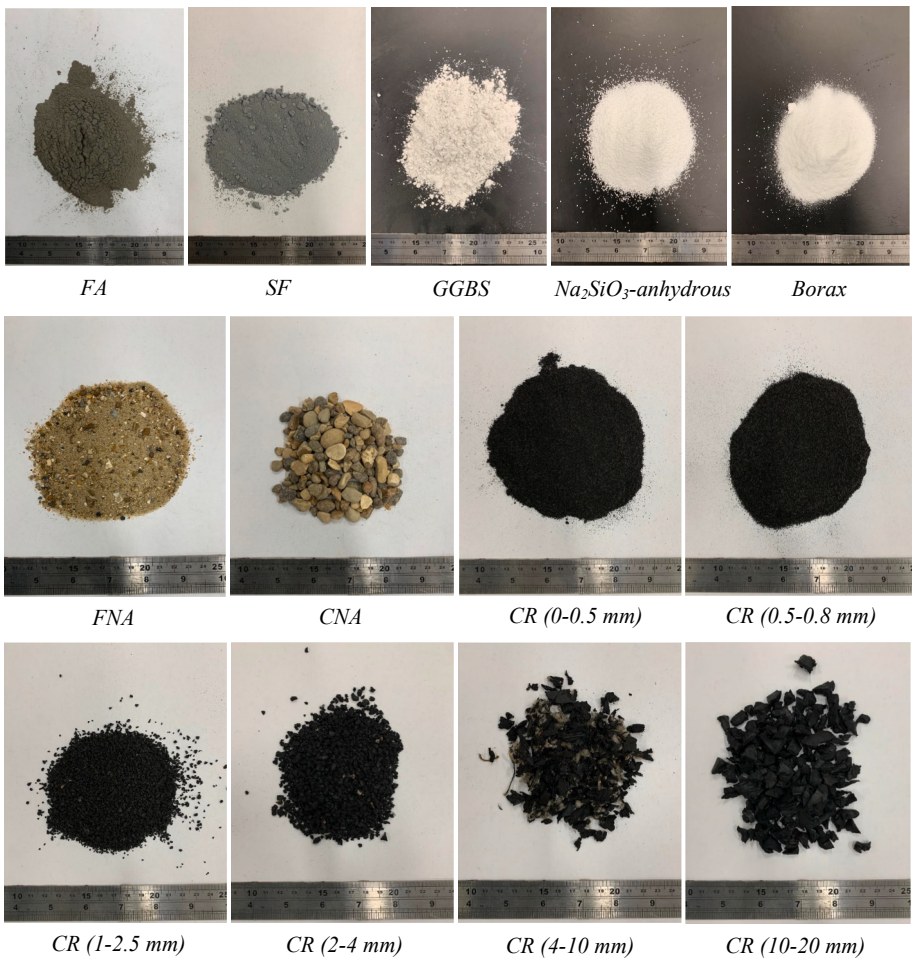


Fig. 1. Raw materials (FA – fly ash, SF – silica fume, GGBS – ground granulated blast furnace slag, Na_2SiO_3-anhydrous – activator, Borax – borax, FNA – fine natural aggregates, CNA – coarse natural aggregates, CR – crumb rubber).

Table 1
Chemical composition of aluminosilicate precursors.

Raw Material	Mass fraction (%)												
	SiO_2	Al_2O_3	Fe_2O_3	CaO	MgO	K_2O	Na_2O	TiO_2	P_2O_5	SO_3	BaO	MnO	LOI
FA	50.62	23.92	11.11	4.51	1.73	3.01	0.81	1.35	0.37	0.67	0.18	0.09	1.63
GGBS	33.43	12.55	0.74	39.87	6.54	0.43	0.18	0.69	0.01	2.48	0.69	0.29	2.10
SF	94.97	1.41	0.23	0.39	0.57	0.96	0.19	0.03	0.09	0.16	–	0.03	0.97

Confined RuC members also perform better in comparison to confined CCM due to the higher confinement activation of the former [52–54]. This makes RuC suitable as a construction material in seismically active regions and as infill material in composite sections. Rubberised alkali-activated concrete (RuAAC) was explored as well over the past few years [55]. A higher replacement of NA with CR particles in RuAAC results in a drop in workability [56,57], a reduction in density [58,59] and a deterioration in mechanical properties [60–62]. Meanwhile, the impact resistance of RuAAC and performance under high-strain rates improve for high CR replacement ratios [58,63].

As indicated, one-part AAMs were formulated using different precursors, solid activators, and admixtures resulting in different strengths and workability performances. In addition, most studies on RuAAC focused on the conventional two-part formulation method, with no study to date providing a detailed assessment of one-part RuAAC, including full stress–strain response, and constitutive models for design purposes are also lacking [55]. This study aims to provide a detailed assessment of the mechanical properties of GGBS- and FA-based one-part RuAAC with up to 60 vol% CR replacement of total NA. The constituent materials of one-part AAC, including precursor content, binder-to-aggregate ratio, solid activator dosage, and admixture dosage, are optimised first to achieve one-part AAC with high strength and flowability. Subsequently, a proportion of the NA is replaced by CR (up to 60 vol%) to form RuAAC, and the elastic modulus, compressive strength, splitting tensile strength, flexural strength, the full constitutive response, and the ultrasonic pulse velocity (UPV), are reported. Analytical expressions and constitutive models to predict the mechanical properties, full stress–strain and flexural stress-crack width responses of one-part RuAAC are provided. Moreover, experimental results on RuC and RuAAC (mostly-two-part RuAAC), available in the literature, were assembled and compared to the results obtained in this study. These were then used to validate the analytical expressions developed in order to examine any possible variations in mechanical properties due to CR addition for different rubberised concrete materials. The study validates one-part RuAAC as a structural concrete material, providing an alternative to cement-based concrete materials and offering a recycling path

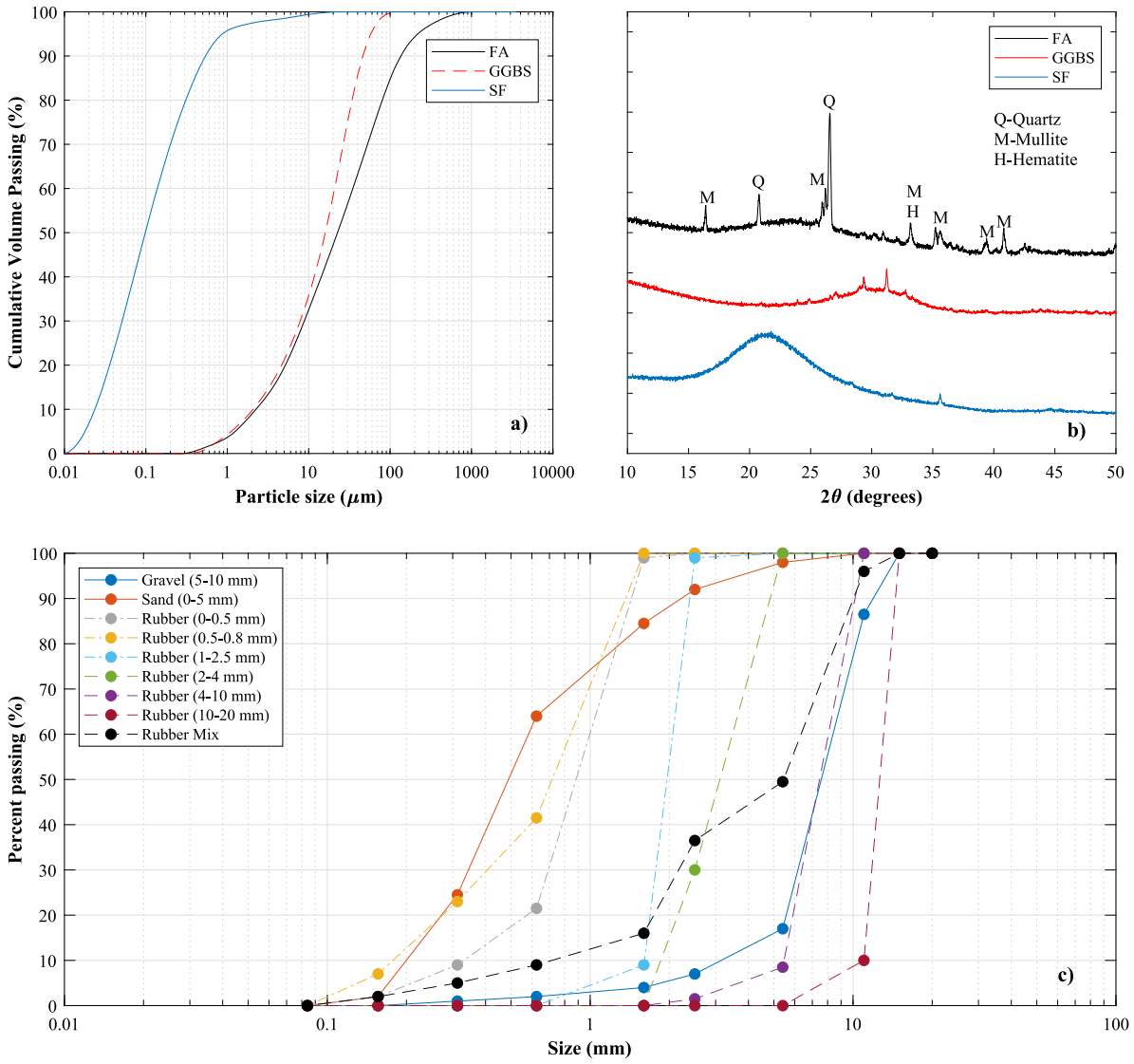


Fig. 2. Material characterization: a) particle size distribution of precursors; b) X-ray diffraction pattern; c) particle size distribution of FNA, CNA and CR particles.

for discarded end-of-life tyres. The results could also encourage further research on structural members using this type of concrete.

2. Materials and methods

2.1. Constituent materials

Fig. 1 depicts macro images of the raw materials used in this study. The main aluminosilicate precursors employed were low calcium FA and GGBS. The specific gravity of the FA and GGBS, determined using an AccuPyc II 1340 pycnometer, was 2.33 and 2.95, respectively. Silica fume (SF) with a specific gravity of 2.38 was also considered by up to 10 % of the binder content. The oxide composition and loss on ignition (LOI) of FA, GGBS and SF – determined using X-ray fluorescence – are given in Table 1. The particle size distribution of the precursors was determined using a Malvern Mastersizer 3000 and the results are given in Fig. 2(a). The median particle size, d_{50}, of FA, GGBS and SF were 22.6, 16 and 0.1 μm, respectively. The crystallinity and phase structure of raw precursors – determined using X-ray diffraction – are shown in Fig. 2(b). The GGBS and SF were mainly amorphous with broad humps in the 26-34° and 16-26° 2θ range, respectively, while the main crystalline peaks in the FA were quartz and mullite. Scanning electron microscope (SEM) images of the precursors are depicted in Fig. 3. FA and SF particles were mainly smooth and spherical, while GGBS particles had a characteristically irregular particle shape.

Granular Na_2SiO_3-anhydrous was used as a solid activator. The modulus of silicate of the activator, as reported by the supplier, was 0.92 (Sodium oxide, Na_2O = 50.2 % and SiO_2 = 46 %). Sodium tetraborate decahydrate-borax ($Na_2B_4O_7{\cdot}10H_2O$) – referred to hereafter as borax – was used as an admixture to improve the fresh properties of the mix. The borax particles had a mesh size of 2.36 mm. The fine natural aggregates (FNA) used in this study were river sand (less than5 mm) with a specific gravity of 2.67 and a water content of 1.34 %. The coarse natural aggregates (CNA) used were crushed gravel (less than10 mm) with a specific gravity of 2.69 and water content of 3 %. CR particles with a specific gravity of 0.97 were used to replace the NA by up to 60 vol%. The CR particles were supplied in different sizes: 0–0.5, 0.5–0.8, 1.0–2.5, 2–4, 4–10 and 10–20 mm, with each specific size making up 5, 5, 15, 20, 10, and 45 % of the total CR replacement, respectively, to ensure a balance between workability and strength loss as suggested by Raffoul et al. [49]. The CR particles were mainly made of carbon black (~25 %), polymers (40–55 %), and softeners and fillers (35–20 %). The particle size distribution of the FNA, CNA and CR particles is given in Fig. 2(c), and an SEM image of the CR blend, depicting their irregular and rough surfaces, is shown in Fig. 3.

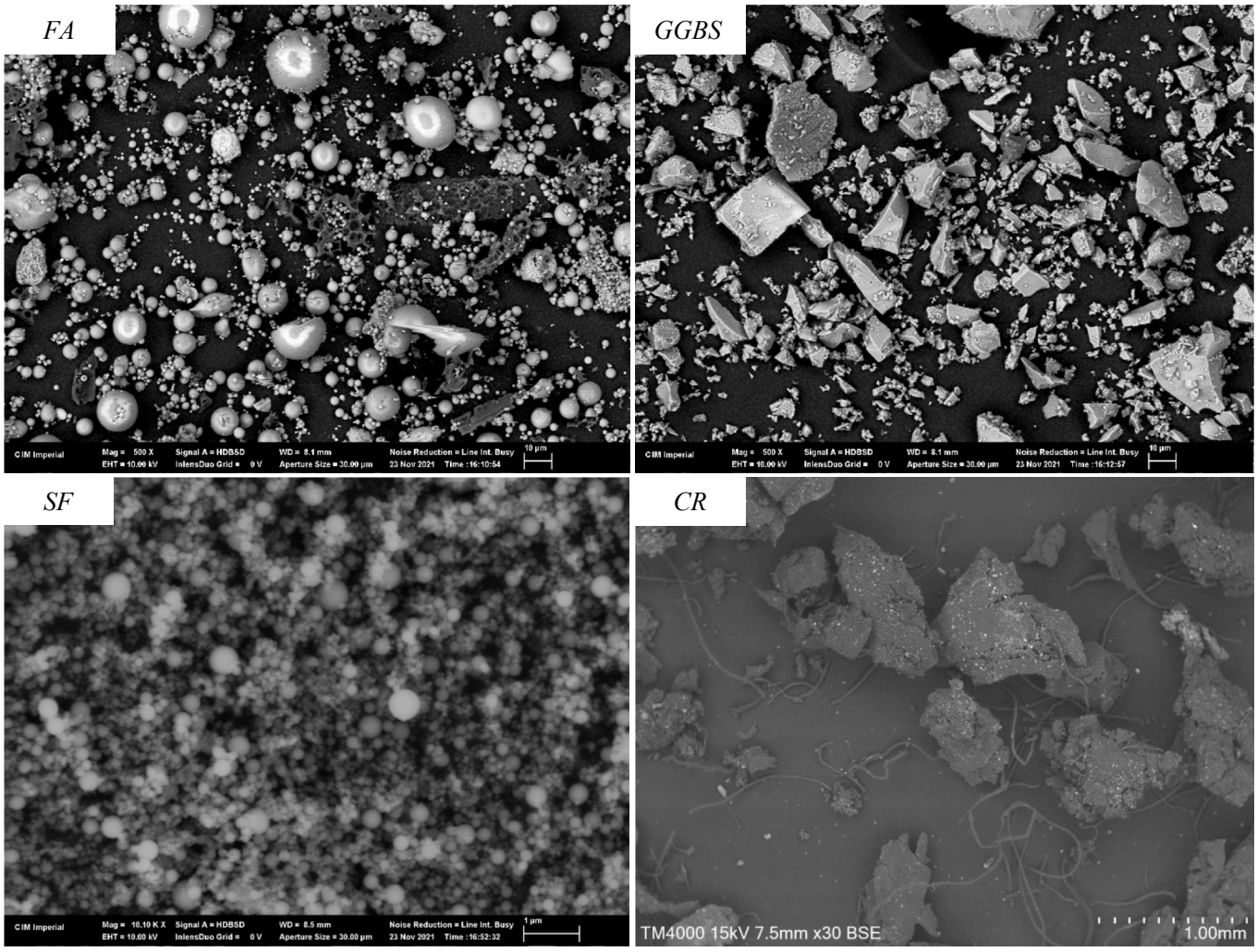


Fig. 3. SEM images of raw precursors and CR particles (FA – fly ash, GGBS – ground granulated blast furnace slag, SF – silica fume, CR – crumb rubber).

2.2. Mix details and procedures

The experimental programme was divided into two stages: a) optimisation and assessment of one-part AAC, and b) assessment of one-part RuAAC. Preliminary pilot mixes were performed to obtain optimal Na_2SiO_3-anhydrous content, borax dosage, and binder-to-aggregate ratio (b/agg). The target 7-day cube compressive strength (100 mm cubes) and slump from the initial pilot trials were 60 MPa and 200 mm, respectively, to achieve normal density high strength concrete with high workability. Twenty-four pilot mixes (*P*1-P24), as listed in Table 2, were investigated with varying activator-to-binder ratios (10 and 12 %), varying borax-to-binder dosages (5 and 6 %), and varying b/agg ratios (0.3 and 0.4). The proportions of FA-to-GGBS investigated in the pilot mixes were 50/50, 20/80 and 0/100. A higher GGBS content was used to achieve the compressive strength target under ambient curing conditions. The water-to-binder content was kept constant at 0.3 following suggestions in the literature [7,8], while the ratio of FNA-to-CNA was kept at 45:55 [48].

After establishing the optimal quantities of Na_2SiO_3-anhydrous, borax and b/agg ratio, six one-part AAC mixes (M1-M6), given in Table 3, were investigated to determine the optimal binder proportions to achieve a concrete slump of 200 mm, a 28-day cylinder compressive strength of 60 MPa, and to observe the strength development up to 90 days. The first three mixes (M1, M2 and M3) had the same FA-to-GGBS ratios used in the pilot mixes. As for mixes M4, M5 and M6, SF was added by 10 wt% of the binder content, while maintaining the FA-to-GGBS ratio as before, giving FA:GGBS:SF proportions of 45:45:10, 72:18:10 and 0:90:10 for M4, M5 and M6, respectively. Five one-part RuAAC mixes were then investigated as given in Table 3. The volumetric rubber replacement ratios, ρ_{vr}, considered were 0 % (M2-R0), 15 % (M2-R15), 30 % (M2-R30), 45 % (M2-R45), and 60 % (M2-R60). The logic behind such replacement ratios was that RuAAC with up to 30 % replacement is likely to achieve strengths suitable for structural applications, while replacements between 30 and 60 % are likely to result in RuAAC with low strength but higher deformation capacity, making it particularly desirable as infill material in confined members. Rubber replacement ratios>60 % were not considered since at such high replacement the behaviour of concrete becomes typically controlled by the rubber.

Mixing of raw materials was conducted in a rotary mixing machine with a capacity of 40 L. The weighted dry materials, including the precursors, Na_2SiO_3-anhydrous, FNA, CNA, CR (if any) and borax, were initially mixed for a total of 5 min as depicted in Fig. 4(a). The FNA and CNA were added to the rotary mixer in a saturated-surface dry condition, while CR particles were added in an air-dry condition. The required amount of water was then added to the mix slowly and mixing was continued for another 5 to 8 min to ensure a homogeneous mix as shown in Fig. 4(b). The fresh concrete was cast in prepared plastic/steel moulds in two or three layers, with each layer being compacted on a vibrating table to remove any entrapped air bubbles. The concrete moulds were then covered with plastic sheets and kept in ambient conditions until demoulding two days after casting. The concrete specimens were then cured in ambient laboratory conditions at a temperature of 20 ± 5 °C

Table 2
Pilot tests mix designs and results.

Mix ID	FA-to-GGBS ratio	FA	GGBS	FNA	CNA	Na_2SiO_3-anhydrous/ binder	Na_2SiO_3-anhydrous	Water/ binder ratio	Water	Borax/ binder	Borax	Slump	7-day ρ[a]	7-day $f_{c,cube}$[a]
–	–	(kg/ m^3)	(kg/ m^3)	(kg/ m^3)	(kg/ m^3)	–	(kg/m^3)	–	(L/ m^3)	–	(kg/ m^3)	(mm)	(kg/m^3)	(MPa)
*P*1	50/50	250	250	750.0	916.7	10 %	50	0.3	150	6 %	30	210	2266 ± 6.65	26.69 ± 1.47
*P*2	20/80	100	400	750.0	916.7	10 %	50	0.3	150	6 %	30	50	2293 ± 8.50	37.54 ± 1.32
*P*3	0/100	0	500	750.0	916.7	10 %	50	0.3	150	6 %	30	7	2311 ± 10.00	46.61 ± 2.00
*P*4	50/50	250	250	750.0	916.7	12 %	60	0.3	150	6 %	30	236	2257 ± 4.00	31.85 ± 0.08
P5	20/80	100	400	750.0	916.7	12 %	60	0.3	150	6 %	30	192	2301 ± 11.50	51.40 ± 0.00
*P*6	0/100	0	500	750.0	916.7	12 %	60	0.3	150	6 %	30	30	2284 ± 3.50	57.93 ± 4.65
P7	50/50	250	250	750.0	916.7	10 %	50	0.3	150	5 %	25	220	2307 ± 12.0	35.14 ± 0.51
P8	20/80	100	400	750.0	916.7	10 %	50	0.3	150	5 %	25	98	2287 ± 1.50	51.72 ± 0.56
P9	0/100	0	500	750.0	916.7	10 %	50	0.3	150	5 %	25	4	2291 ± 9.00	52.67 ± 0.18
P10	50/50	250	250	750.0	916.7	12 %	60	0.3	150	5 %	25	232	2291 ± 1.00	36.35 ± 0.57
P11	20/80	100	400	750.0	916.7	12 %	60	0.3	150	5 %	25	55	2262 ± 4.00	53.55 ± 0.27
P12	0/100	0	500	750.0	916.7	12 %	60	0.3	150	5 %	25	23	2309 ± 11.50	58.62 ± 0.04
P13	50/50	300	300	675.0	825.0	10 %	60	0.3	180	6 %	36	233	2244 ± 10.00	37.87 ± 0.77
P14	20/80	120	480	675.0	825.0	10 %	60	0.3	180	6 %	36	231	2284 ± 10.00	52.45 ± 1.03
P15	0/100	0	600	675.0	825.0	10 %	60	0.3	180	6 %	36	13	2274 ± 9.00	57.04 ± 0.10
P16	50/50	300	300	675.0	825.0	12 %	72	0.3	180	6 %	36	259	2260 ± 2.00	37.46 ± 0.52
P17	20/80	120	480	675.0	825.0	12 %	72	0.3	180	6 %	36	252	2275 ± 14.00	56.33 ± 1.28
P18	0/100	0	600	675.0	825.0	12 %	72	0.3	180	6 %	36	244	2316 ± 2.00	66.40 ± 0.46
P19	50/50	300	300	675.0	825.0	10 %	60	0.3	180	5 %	30	261	2218 ± 1.50	33.02 ± 1.61
P20	20/80	120	480	675.0	825.0	10 %	60	0.3	180	5 %	30	238	2267 ± 15.50	53.07 ± 0.06
*P*21	0/100	0	600	675.0	825.0	10 %	60	0.3	180	5 %	30	10	2301 ± 1.00	66.24 ± 0.78
P22	50/50	300	300	675.0	825.0	12 %	72	0.3	180	5 %	30	252	2251 ± 7.50	40.50 ± 0.05
*P*23	20/80	120	480	675.0	825.0	12 %	72	0.3	180	5 %	30	242	2300 ± 18.70	62.60 ± 2.04
P24	0/100	0	600	675.0	825.0	12 %	72	0.3	180	5 %	30	48	2251 ± 14.57	66.42 ± 2.13

[a] *Results are the average of two values.*

Table 3
Mix design proportions for one-part AAC and one-part RuAAC.

Mix ID	FA-to-GGBS ratio	FA	GGBS	SF	Na_2SiO_3-anhydrous	FNA	CNA	CR	Borax	Water
(-)	(-)	(kg/m^3)	(kg/m^3)	(kg/m^3)	(kg/m^3)	(kg/m^3)	(kg/m^3)	(kg/m^3)	(kg/m^3)	(L)
M1	50/50	300	300	0	72	675	825	–	30	180
M2	20/80	120	480	0	72	675	825	–	30	180
M3	0/100	0	600	0	72	675	825	–	30	180
M4	50/50	270	270	60	72	675	825	–	30	180
M5	20/80	108	432	60	72	675	825	–	30	180
M6	0/100	0	540	60	72	675	825	–	30	180
M2-R0	20/80	120	480	0	72	675.0	825.0	0.0	30	180
M2-R15	20/80	120	480	0	72	573.8	701.3	81.4	30	180
M2-R30	20/80	120	480	0	72	472.5	577.5	162.8	30	180
M2-R45	20/80	120	480	0	72	371.3	453.8	244.2	30	180
M2-R60	20/80	120	480	0	72	270.0	330.0	325.6	30	180

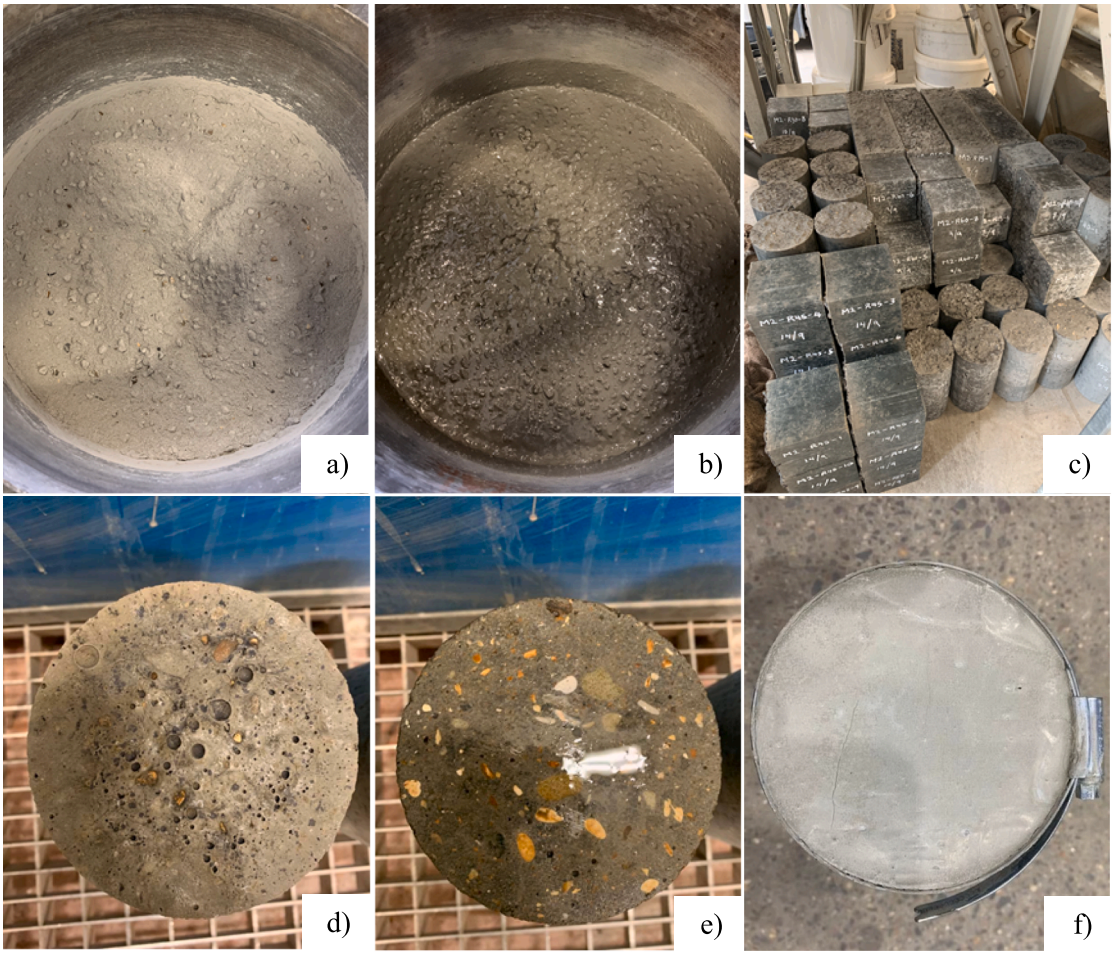


Fig. 4. Mixing of raw materials and specimens' preparation: a) dry mixing, b) wet mixing; c) curing at ambient conditions; d) cylindrical specimen prior to grinding; e) specimen after water grinding; f) fitting with jubilee ring and capping with high-strength mortar.

and relative humidity of 50 ± 20 % until testing as shown in Fig. 4(c). Prior to testing, all non-rubberised cylindrical specimens (Fig. 4(d)) tested in compression were ground in a water grinding machine as depicted in Fig. 4(e) to ensure smooth contact with the testing machine. As for rubberised cylindrical specimens tested in compression, and due to the difficulty of grinding rubberised surfaces, their ends were fitted with jubilee rings and their top surface was capped with high-strength mortar, as shown in Fig. 4(f), to ensure a level surface and to avoid local crushing or failure at the ends of the specimens.

2.3. Testing arrangements and specimen details

The fresh properties for each mix were determined immediately after mixing using a concrete slump test following BS EN 12350–2 [64]. The slump cone had a base and top diameter of 200 mm and 100 mm, respectively, and a height of 300 mm. The cone was filled in three layers, and each layer was struck 25 times using a circular metal rod with a 600 mm length and a 16 mm diameter. The hardened density and compressive strength of the pilot mixes (Table 2) were determined from 100 × 100 × 100 mm cube specimens at 7 days to obtain a balance between strength and workability. A total of forty-eight cubic specimens covering twenty-four pilot mixes, with two identical specimens for each mix, were examined to give an indication of strength properties. The hardened density, compressive strength, as well as UPV, of the one-part AAC mixes (M1-M6) in Table 3 were determined from a total of fifty-four 100 × 100 × 100 mm cube specimens tested at 7, 28 and 90 days. Additionally, eighteen ϕ100 × 200 mm cylindrical specimens were tested at 28 days for UPV and full stress–strain response. The density, UPV and compressive strength of the one-part RuAAC mixes (M2-R0 – M2-R60) in Table 3 were determined from a total of forty-five 100 × 100 × 100 mm cube specimens tested at 7, 28 and 90 days. An additional thirty ϕ100 × 200 mm cylindrical specimens were tested for UPV, full stress–strain response and splitting tensile strength at 28 days, while a total of fifteen 100 × 100 × 350 mm concrete prisms were tested for flexural strength at 28 days. The results of the one-part AAC mixes and one-part RuAAC mixes in Table 3 were determined from an average of three identical specimens. The hardened density of different specimens was determined following BS EN 12390–7 [65] by dividing the specimen mass by its volume.

The testing arrangements employed for the assessment of mechanical properties are shown in Fig. 5. The compressive strength was determined using an Automax machine with a 3000 kN capacity as shown in Fig. 5(a) following BS EN 12390–3 [66]. The test was performed in load control conditions at a loading rate of 0.3 MPa/s. The full stress–strain response of one-part AAC and one-part RuAAC specimens was conducted under displacement control conditions. The test was carried out in an Instron Satec 3500 kN machine at a displacement rate of 0.25 mm/min. The specimens were placed at the bottom platform of the testing machine, and steel loading plates of 100 mm diameter were placed at the top and bottom of the specimens as depicted in Fig. 5(d). The bottom loading plate was 50 mm thick, while the top loading plate was 75 mm thick and was fitted with a 3D rotating hinge to prevent any loading eccentricity. The pre-peak axial behaviour was determined from three vertical displacement transducers placed at 120° around the specimen.

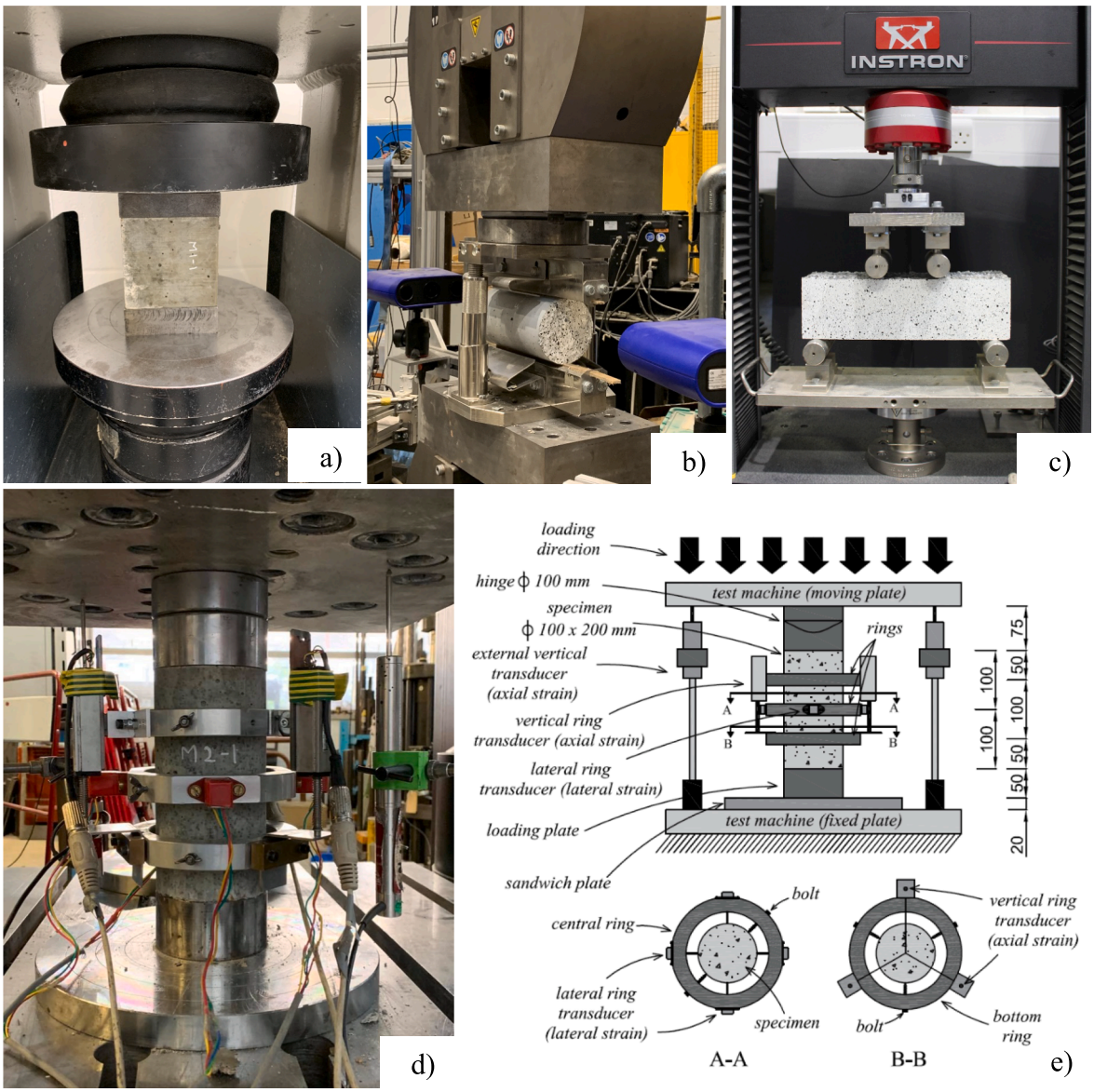


Fig. 5. Test setups: a) cube compressive strength, b) splitting tensile strength, c) flexural strength, d) cylinder stress–strain response, e) layout of cylinder stress–strain test.

These transducers were connected to two circular steel rings placed symmetrically around the specimen covering the middle 100 mm as illustrated in Fig. 5(e). The steel rings were connected to the cylindrical specimen via three steel bolts. Two other displacement transducers were placed directly on the loading platen of the Instron machine to measure the displacement in the post-peak regime. A third circular ring with four lateral displacement transducers spaced at 90° apart was placed at the middle of the specimen to measure the lateral displacement. All displacement transducers were connected to a datalogger to record the results in real time. Displacement values recorded from the transducers were averaged and converted to strains according to the appropriate gauge length to assess the stress–strain response.

The splitting tensile strength test was performed in an Instron Satec 600 kN machine as shown in Fig. 5(b). The test was conducted following BS EN 12390–6 [67] in displacement control conditions at a rate of 0.1 mm/min. As for the flexural strength, the test was carried out in an Instron 100 kN machine as shown in Fig. 5(c) following BS EN 12390–5 [68]. The flexural prisms were loaded under four-point bending in displacement-control conditions at a rate of 0.1 mm/min. The distance between the two loading points was 100 mm while the distance between the supports was 300 mm. For both the splitting strength cylinders and flexural prisms, digital image correlation (DIC) was used to determine the surface displacements as loading was applied. In the case of the splitting strength cylinders, two 2-megapixel (MP) cameras were placed at each end, while for the flexural prisms, two 5MP cameras with 35 mm f/2D lenses were placed facing one side of the prism. Prior to any recordings, the ends of the splitting strength cylinders and the surface of the flexural prisms facing the cameras were painted white and then carefully speckled with black dots (~0.5–2.0 mm in diameter) to form a contrasting black-and-white pattern. A calibration procedure, as recommended by the manufacturer [69], was employed to ensure accurate measurements. Images were then taken as the load was applied at a rate of 2 Hz. The DIC data was processed using a LaVision DaVis 10.2 software [70], and crack widths were determined using a virtual extensometer of 50 mm length placed across the crack.

UPV readings were recorded for compressive strength specimens, both cubes and cylinders, prior to crushing using a Proceq Pundit 200 UPV testing machine as shown in Fig. 6. The test system consisted of a control box containing a display device, a pulse generator, a timing circuit, and two transducers connected to the control box via cables. The

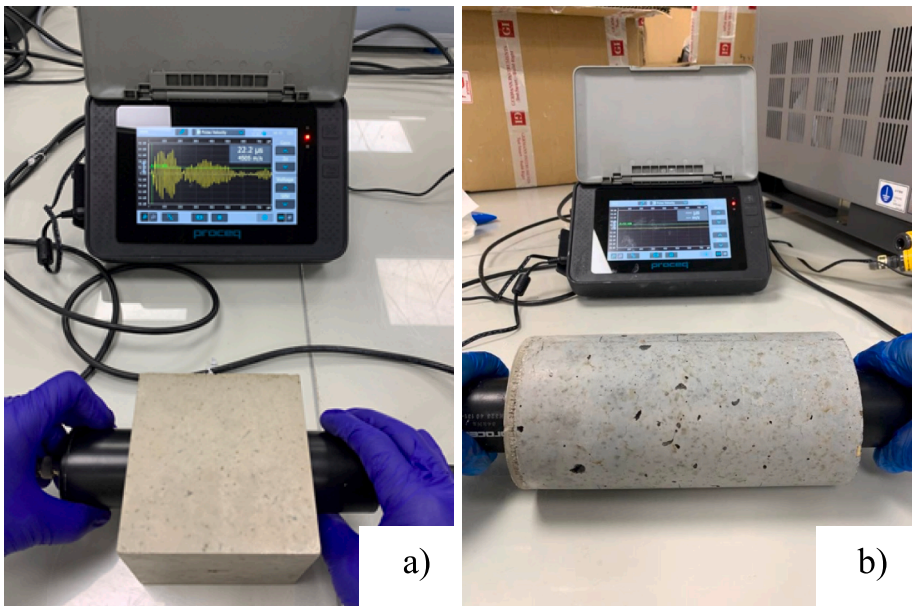


Fig. 6. UPV test: a) concrete cube, b) concrete cylinder.

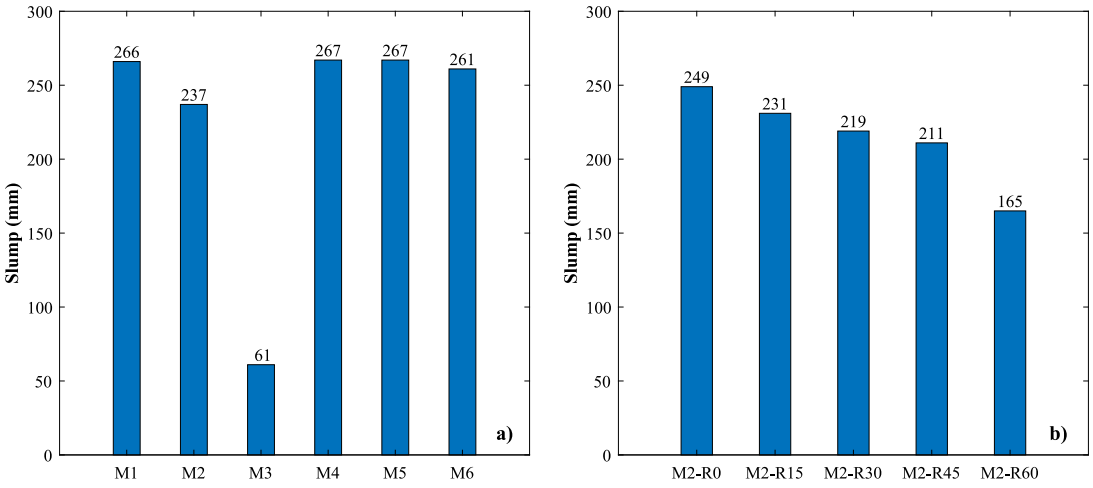


Fig. 7. Concrete slump results: a) one-part AAC, b) one-part RuAAC.

transduces had a frequency of 54 kHz ± 5 kHz and a surface diameter of 36.8 mm. The contact surface of the transducers was greased with coupling gel, and a minimum of three readings were taken for each specimen. UPV results can give an indication of the specimen compressive strength, internal cracks, voids, and overall uniformity [71]. Due to slower ultrasonic wave propagation in liquid and gas phases, a lower UPV typically indicates the presence of cracks and discontinuities within the cement matrix [72].

3. Assessment of one-part AAC

3.1. Mix optimisation

The concrete slump results, 7-day density (ρ), and 7-day cube compressive strength ($f_{c,cube}$) for the pilot mixes are given in Table 2. The results indicate that for the same Na_2SiO_3-anhydrous content, borax dosage and b/agg ratio, a higher GGBS content in the mix results in a higher 7-day $f_{c,cube}$ and a lower slump, which is in agreement with the literature [15,16,25,33]. For instance, *P*1 and *P*3 specimens with FA-to-GGBS ratios of 50:50 and 0:100, respectively, achieved a 7-day $f_{c,cube}$ of 26.7 and 46.6 MPa, indicating a 74.5 % increase in $f_{c,cube}$ with higher GGBS content. This increase in $f_{c,cube}$ is due to the higher CaO content of GGBS in comparison to FA, which readily releases Ca^{+2} and forms C-A—S—H gels in alkaline environments. Meanwhile, the slump of *P*1 and *P*3 was 210 and 7 mm, respectively, corresponding to a reduction of nearly 96.7 %. The reduction in flowability due to higher GGBS can be attributed to their irregular particle shape prohibiting inter-particle rollover [73], and their quick reactivity [74]. In contrast, FA particles are spherical, react slowly and disperse readily in alkaline environments, which results in better flow [74].

For mixes with the same FA-to-GGBS ratio, borax dosage, and b/agg ratio, a relatively high Na_2SiO_3-anhydrous content resulted in a high concrete slump and 7-day $f_{c,cube}$. For example, comparing *P*1 and *P*4 it is shown that an increase in the activator-to-binder content from 10 to 12 % led to an enhancement in the concrete slump and 7-day $f_{c,cube}$ by 12 and 19 %, respectively. The results are in agreement with previous work [8,75], where the compressive strength, f_c, generally increased with the activator content. This can be attributed to a rise in pH with higher activator dosage, followed by higher dissolution of Si/Al/Ca species from the precursors and the formation of more binding phases. In

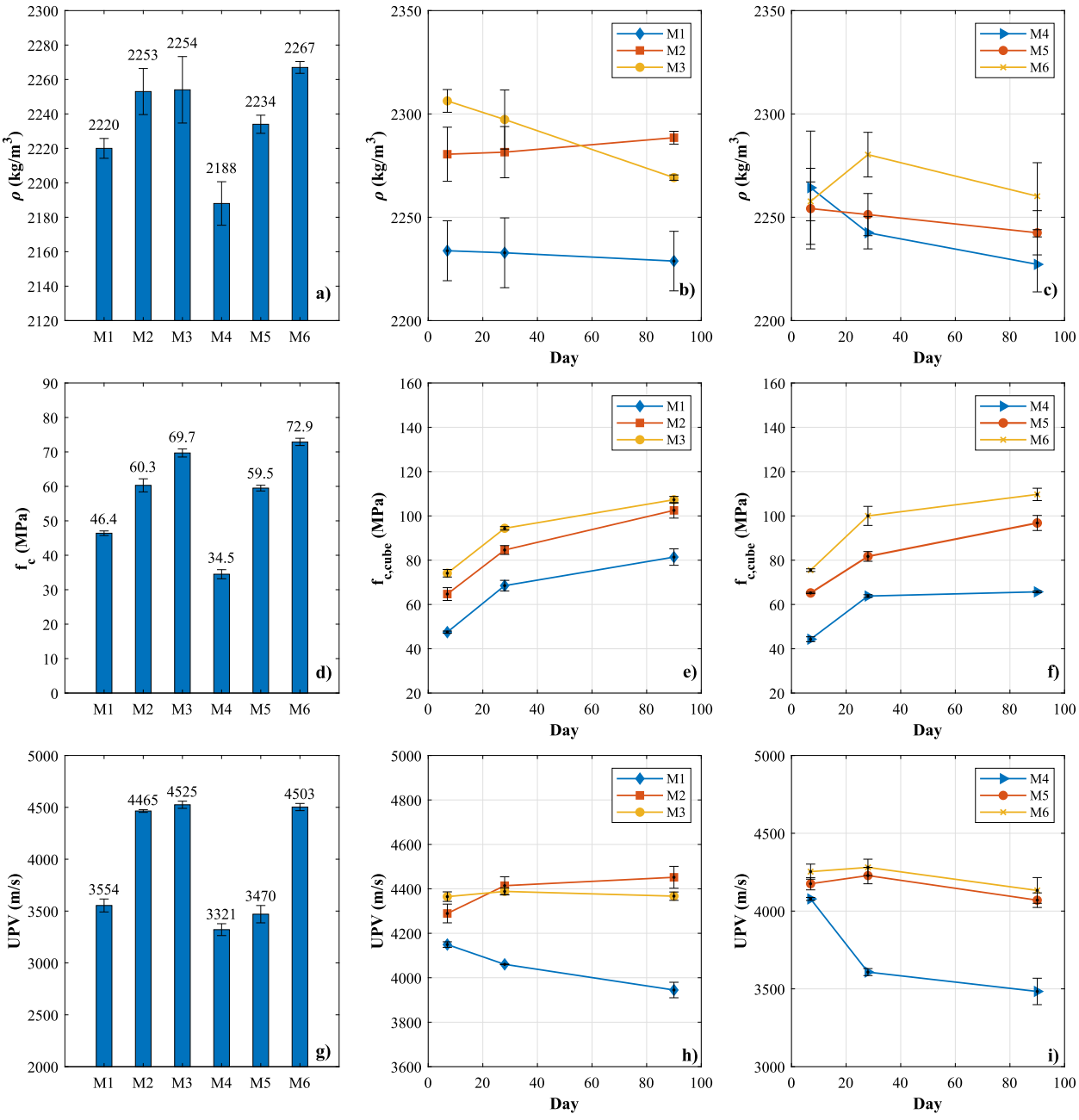


Fig. 8. One-part AAC results: a-c) concrete ρ, d-f) f_c, g-i) UPV.

addition, a higher Na_2SiO_3-anhydrous dosage plasticizes the mix and causes lower yield stress at early ages, resulting in an improved concrete slump [76].

Reducing the borax dosage from 6 to 5 % while keeping the FA-to-GGBS ratio, Na_2SiO_3-anhydrous content, and b/agg ratio constant generally led to an increase in the 7-day $f_{c,cube}$. For example, P15 with 6 % borax dosage achieved a 7-day $f_{c,cube}$ of 57.04 MPa, while *P*21 with a 5 % borax dosage achieved a 7-day $f_{c,cube}$ of 66.24 MPa. As for the concrete slump, the results were inconclusive and varied from one mix to the other. This negative effect of high amounts of borax on $f_{c,cube}$ was also reported previously by Oderji et al. [7].

Increasing the b/agg ratio from 0.3 to 0.4 resulted in an improved concrete slump and 7-day $f_{c,cube}$. For instance, while keeping all other parameters constant, the concrete slump of *P*1 (b/agg = 0.3) and P13 (b/agg = 0.4) was 210 and 233 mm, respectively, corresponding to an 11 % overall increase. The 7-day $f_{c,cube}$ of *P*1 and P13 was 26.7 and 37.9 MPa, respectively, indicating a 42 % increase. This is understandable as a higher b/agg ratio means a higher Na_2SiO_3-anhydrous content, borax dosage and water (all are tied to the binder content), which produces enhanced lubrication of aggregates and greater concrete flow. Also, a greater amount of aluminosilicate precursors and Na_2SiO_3-anhydrous content due to higher b/agg ratio results in greater dissolution of Si/Al ions and formation of C-A—S—H and *N*-A—S—H gels.

In mixes P10-P12 (b/agg = 0.3) and mixes P22-P24 (b/agg = 0.4), the Na_2SiO_3-anhydrous content was 12 % while the borax dosage was 5 %. This in turn resulted in the highest observed 7-day $f_{c,cube}$ for a given b/agg ratio. For instance, comparing mixes P10-P12 to *P*1-*P*3, the increase in the 7-day $f_{c,cube}$ was in the range of 26–43 %, while mixes P22-P24 showed a 7-day $f_{c,cube}$ increase in the range of 7–19 % when compared to P13-P15. Similarly, the slump of mixes P10-P12 and P22-P24 was higher than mixes *P*1-*P*3 and P13-P15, respectively. The 7-day concrete ρ of the pilot mixes generally increased with higher

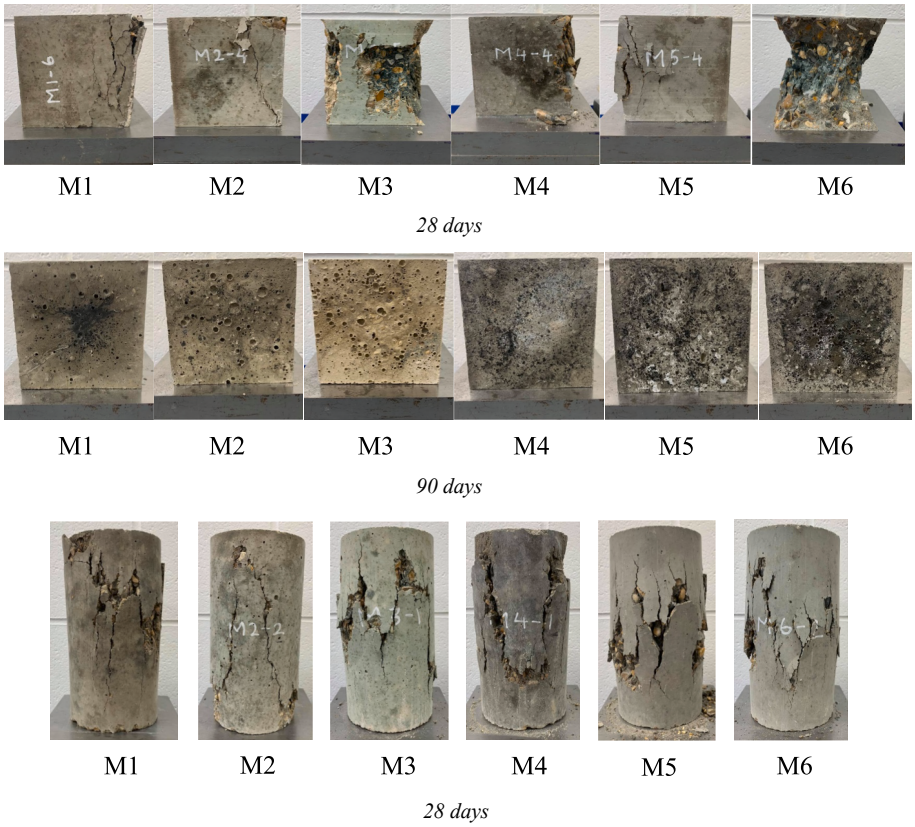


Fig. 9. Failure and visual appearance of one-part AAC specimens (refer to Table 3 for mix details).

Table 4
Summary of 28-day test results.

Mix ID	f_c	$f_{c,cube}$	$f_c/f_{c,cube}$	$\varepsilon_{cr,1}$	$\varepsilon_{cr,2}$	E_c	G_c	f_{sp}	f_f	$G_{c\text{-}sp}$	$G_{c\text{-}f}$
(-)	(MPa)	(MPa)	(-)	(‰)	(‰)	(GPa)	(N/mm^2)	(MPa)	(MPa)	(N/mm)	(N/mm)
M1	46.36 ± 0.66	68.53 ± 2.41	0.68	3.19 ± 0.05	−2.48 ± 0.22	17.39 ± 0.13	0.108 ± 0.002	–	–	–	–
M2	60.33 ± 1.90	84.63 ± 2.03	0.71	2.53 ± 0.24	−1.85 ± 0.14	27.69 ± 2.68	0.123 ± 0.009	–	–	–	–
M3	69.71 ± 1.19	94.45 ± 0.85	0.74	2.97 ± 0.07	−1.92 ± 0.24	26.35 ± 1.78	0.151 ± 0.009	–	–	–	–
M4	34.51 ± 1.32	63.81 ± 0.57	0.54	3.67 ± 0.60	−5.37 ± 0.90	11.24 ± 1.91	0.109 ± 0.012	–	–	–	–
M5	59.49 ± 0.83	81.71 ± 2.22	0.73	3.26 ± 0.26	−2.97 ± 0.18	21.08 ± 1.46	0.151 ± 0.003	–	–	–	–
M6	72.93 ± 1.06	99.97 ± 4.26	0.73	3.16 ± 0.25	−2.31 ± 0.45	23.50 ± 2.49	0.199 ± 0.005	–	–	–	–
M2-R0	80.38 ± 2.71	98.30 ± 0.74	0.82	3.16 ± 0.18	−1.57 ± 0.26	28.31 ± 0.50	0.203 ± 0.041	4.61 ± 0.33	3.52 ± 0.15	–	1.80 ± 0.52
M2-R15	42.04 ± 2.01	70.28 ± 1.56	0.60	2.89 ± 0.14	−1.62 ± 0.08	17.98 ± 0.00	0.111 ± 0.011	4.15 ± 0.70	3.40 ± 0.31	8.79 ± 1.11	1.55 ± 0.30
M2-R30	20.59 ± 0.68	45.55 ± 0.78	0.45	2.87 ± 0.08	−1.90 ± 0.79	10.14 ± 1.69	0.101 ± 0.043	2.87 ± 0.23	3.07 ± 0.16	3.40 ± 0.68	1.72 ± 0.49
M2-R45	14.69 ± 1.35	27.96 ± 1.27	0.53	2.71 ± 0.46	−1.91 ± 0.35	7.88 ± 2.37	0.093 ± 0.019	2.05 ± 0.06	2.36 ± 0.11	1.51 ± 0.18	0.72 ± 0.11
M2-R60	10.92 ± 0.35	18.03 ± 0.63	0.61	2.45 ± 0.47	−2.04 ± 0.25	5.96 ± 0.46	0.074 ± 0.009	1.56 ± 0.13	1.89 ± 0.16	1.27 ± 0.29	1.00 ± 0.20

GGBS content due to its higher specific gravity, but this was not always the case. The 7-day ρ of the pilot specimens ranged from 2218 (P19) to 2316 kg/m^3 (P18), indicating typical values for normal weight concrete. Given the concrete slump and 7-day $f_{c,cube}$ targets of 200 mm and 60 MPa, respectively, the optimum activator-to-binder content, borax-to-binder dosage and b/agg ratio were taken as 12 %, 5 % and 0.4, respectively (P22-P24). These correspond to mixes M1-M3, respectively, that are studied in detail in Sections 3.2-3.5.

3.2. Fresh and physical properties

The concrete slump results of the one-part AAC mixes M1-M6 are depicted in Fig. 7 showing a similar trend to that of the pilot mixes. As indicated in Fig. 7(a), a high GGBS content in the mix led to a low concrete slump. Meanwhile, adding SF by 10 % of binder content had a positive effect on the concrete slump. For the same FA-to-GGBS ratio, adding SF caused the slump to increase from 237 to 267 mm (M2 versus

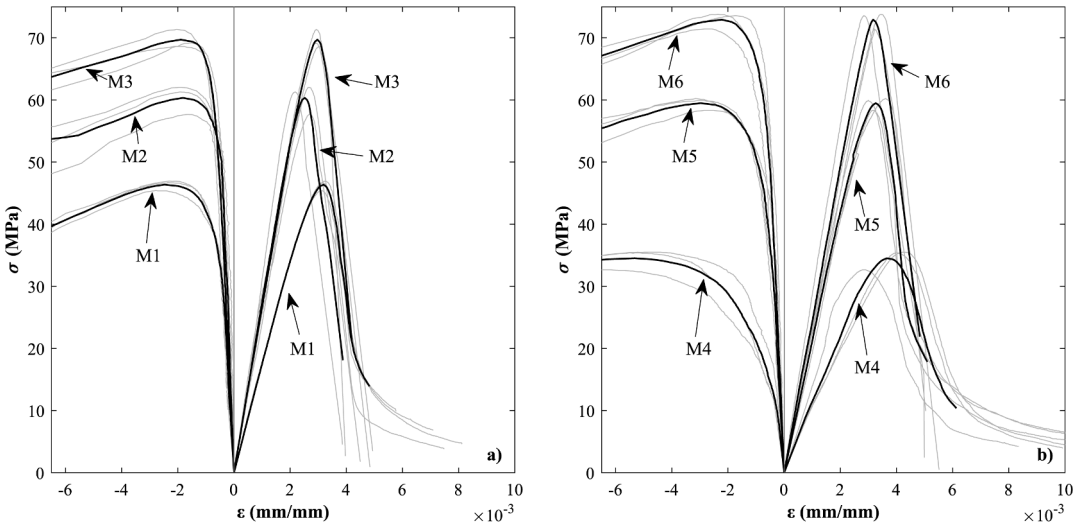


Fig. 10. Comparison of σ-ε response of one-part AAC specimens: a) mixes M1-M3, b) mixes M4-M6.

M5). The effect of SF was more notable when comparing M3 and M6, where the slump quadrupled from 61 mm to 261 mm. This improvement in concrete flow due to SF addition in GGBS-based one-part AAMs was observed before [17], and is mainly attributed to enhanced repulsion between cementitious particles [77].

The 28-day ρ of mixes M1-M6 determined from the cylindrical specimens is shown in Fig. 8(a) to vary between 2188 and 2267 kg/m^3 in proportion with the GGBS content. For instance, the 28-day ρ of M3 was 1.5 % higher than that of M1, and the 28-day ρ of M6 was 3.6 % higher than M4. The ρ values determined from the cube specimens for up to 90-days are shown in Fig. 8(b) for M1-M3 and Fig. 8(c) for M4-M6. Considering M1-M3, M3 with the highest GGBS content had the highest density at 7- and 28-days compared with M2 and M3. However, over the 83-day period (from 7-days to 90-days), M3 and M1 experienced a minor reduction in ρ of about 1.6 and 0.2 %, respectively; while M2 experienced a slight increase in ρ over the same period (0.35 %). This caused the ρ of M2 to be slightly higher than that of M3 at 90-days. Looking at the results of M4-M6, both M4 and M5 experienced a minor drop in ρ from 7- to 90-days, while M6 experienced an initial increase in ρ from 7- to 28-days, followed by a drop from 28- to 90-days of about 0.9 %.

A reduction in concrete ρ over time is typically associated with evaporation of water as the concrete dries. Another reason for the reduction in ρ in AAC could be efflorescence. As shown in Fig. 9, mixes M1-M3 did not show any signs of efflorescence (i.e., white deposits that appear on the surface due to activator leaching and reacting with atmospheric CO_2). Meanwhile, mixes M4-M6 had white deposits on their surface after 90 days of curing. The white deposits were more significant in mixes M4 and M5, possibly due to their reduced reactivity, causing the excess solid activator to leach to the surface and react with the surrounding CO_2.

3.3. Compressive strength

The 28-day cylinder f_c of specimens M1-M6 is given in Fig. 8(d). The strength increased proportionally with the amount of GGBS due to a higher dissolution and geopolymerization under ambient curing conditions. Meanwhile, the addition of SF in FA and GGBS mixes resulted in a reduction in f_c. For instance, M4 and M5 achieved 28-day cylinder f_c that was 25.6 and 1.3 % lower than that of M1 and M2, respectively. In contrast, adding SF to the mixes with only GGBS resulted in a slight improvement in f_c. M6 achieved a 4.6 % higher 28-day cylinder f_c when compared to M3. The same trend was seen for the 28-day cubic strengths depicted in Fig. 8(e) and Fig. 8(f). This is in agreement with the observation of Dong et al. [8] where SF addition caused a reduction in the reactivity of FA and GGBS-based one-part AAMs; while it increased the rate of C-A—S—H gel formation for GGBS-based one-part AAM [8].

Fig. 8(e) and Fig. 8(f) illustrate the cube compressive strength development up to 90 days for mixes M1-M3 and M4-M6, respectively. Regardless of the mix design, $f_{c,cube}$ increased up to 90-days, albeit at different rates. The increase in $f_{c,cube}$ was higher from 7- to 28-days than from 28- to 90-days for all mixes. The highest increase in $f_{c,cube}$ from 7- to 28-days was observed in mix M1 (by 44.4 %), while the highest increase in $f_{c,cube}$ from 28- to 90-days was observed for mix M2 (by 21.1 %). The lowest increase in $f_{c,cube}$ from 7- to 28-days and from 28- to 90-days was for mixes M5 (by 25.3 %) and M4 (by 2.9 %), respectively. A higher increase in $f_{c,cube}$ over time in AAC indicates stable formation of hydration products, and all mixes appeared to show stable development in f_c over the 90-day period. The 28-day cylinder-to-cube compressive strength ratio ($f_c/f_{c,cube}$) of mixes M1-M6 is reported in Table 4. The ratio was generally around 70 %, except for M4 which had a 28-day $f_c/f_{c,cube}$ of 54 %. This is lower than that for conventional normal strength concrete where $f_c/f_{c,cube}$ is usually around 80 %.

The failure patterns of the cubes and cylinders of mixes M1-M6 tested in compression at 28 days are shown in Fig. 9. Most cube specimens showed vertical cracks along the direction of load initiated diagonally from the cube ends at an angle of 45-60° from the horizontal. This diagonal inclination is due to shear stress on the top and bottom surface of the specimens induced by end friction between the loading platens and the specimens. The cylinders shown in Fig. 9 displayed cone-shaped failure patterns with preserved top and bottom surfaces, due to combined shear failure and tensile splitting.

3.4. Stress–strain response

The average 28-days stress–strain (σ-ε) curves of mixes M1-M6, obtained from three tests, are depicted in Fig. 10 by black lines and the main results are given in Table 4. It is shown that an increase in the GGBS content resulted in a proportional increase in the elastic modulus E_c, a reduction in the axial crushing strain, $\varepsilon_{cr,1}$, and lateral crushing strain, $\varepsilon_{cr,2}$. For example, E_c improved by nearly 51.5 % from 17.4 to 26.4 GPa when comparing mixes M1 to M3, respectively. Despite the lower GGBS content and f_c of M2 when compared to M3, it attained a higher E_c (27.7 GPa), and lower $\varepsilon_{cr,1}$ and $\varepsilon_{cr,2}$. M2 achieved the highest E_c and lowest $\varepsilon_{cr,1}$ and $\varepsilon_{cr,2}$ among all the 6 mixes investigated, followed by M3 and M6. The results indicate that a higher FA content in the mix causes a reduction in stiffness, but when added in small amounts (20 % of binder content), an improvement in stiffness occurs, which could be

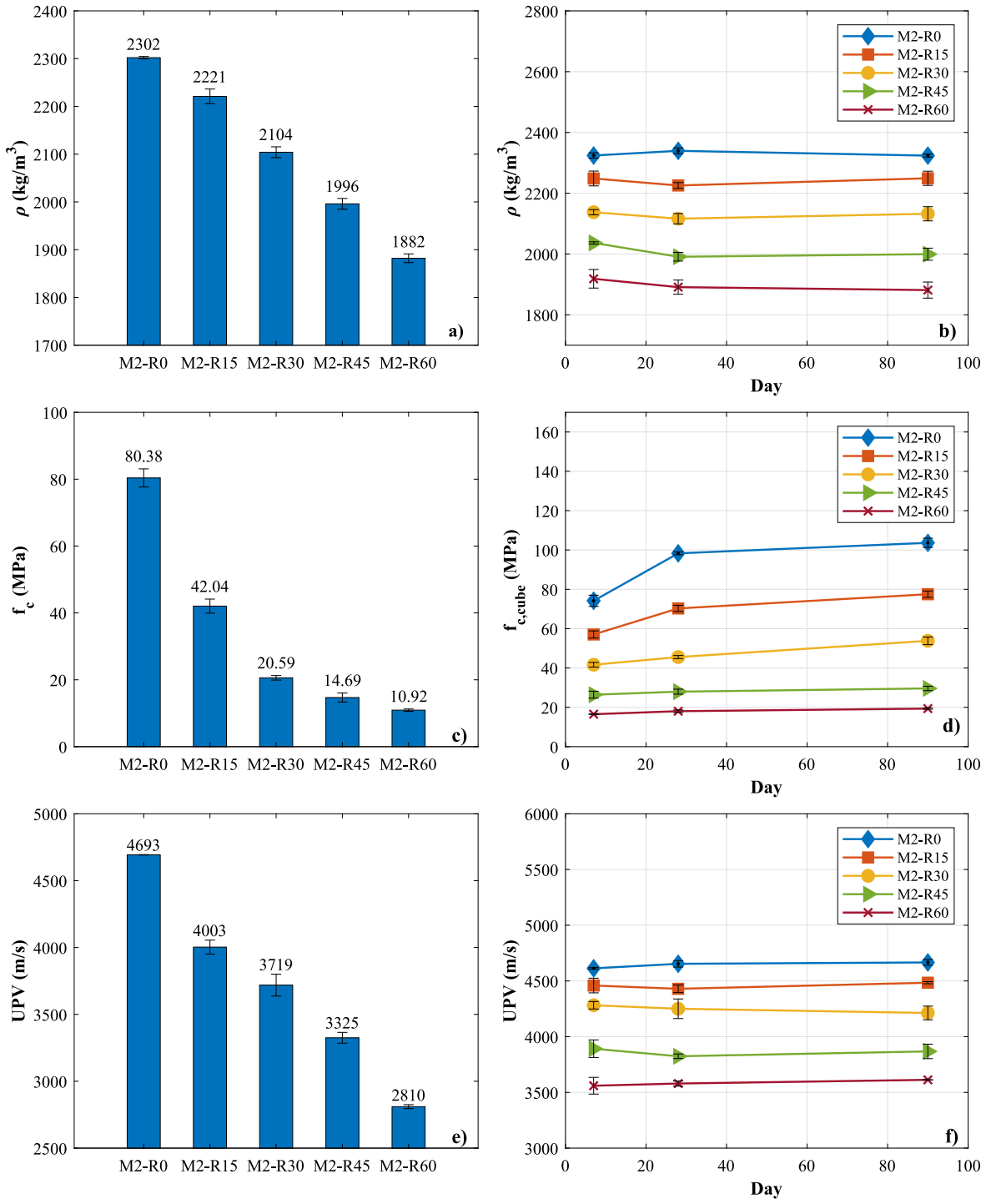


Fig. 11. One-part RuAAC results: a) 28-day ρ of concrete cylinders b) ρ of concrete cubes, c) 28-day f_c of concrete cylinders, d) $f_{c,cube}$, e) 28-day UPV of concrete cylinders, f) UPV of concrete cubes.

attributed to optimum compatibility between different binder proportions. Adding SF by 10 % of binder content caused a reduction in E_c, and an increase in $\varepsilon_{cr,1}$ and $\varepsilon_{cr,2}$. This reduction in E_c due to SF addition is due to the quicker reaction of solid activator with SF particles which reduces the reactivity of FA and results in more FA unreacted particles.

A higher GGBS content in the mix resulted in higher crushing energy, G_c, taken as the area under the σ-ε curve as shown in Fig. 13(e) and given in Table 4. For instance, G_c of mixes M1 and M3 were 0.108 and 0.151 N/mm^2, respectively, indicating an increase of 39.8 % between the two mixes. The increase in G_c with greater GGBS content was even higher for the mixes M4-M6, where G_c rose by nearly 82.6 % from 0.109 to 0.199 N/mm^2 for M4 and M6, respectively. The incorporation of SF in the mix caused G_c to increase as well. For example, comparing M2 to M5, the addition of SF caused G_c to increase from 0.123 to 0.151 N/mm^2.

3.5. Ultrasonic pulse velocity

The UPV results of concrete cylinders at 28 days is shown in Fig. 8(g). The UPV readings for the cylindrical specimens ranged from 3554 to 4525 m/s for mixes M1-M3 and 3321–4503 m/s for mixes M4-M6. The

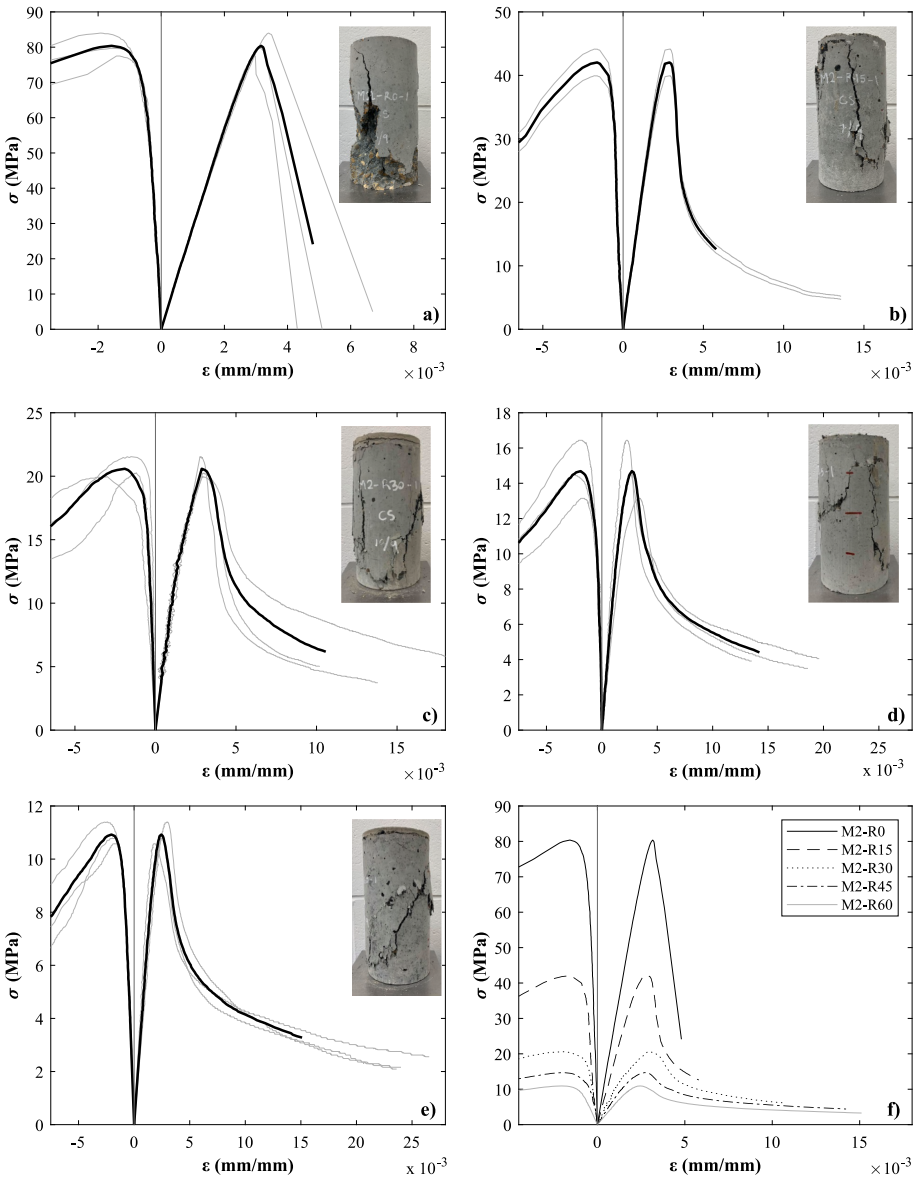


Fig. 12. Stress–strain response of One-part RuAAC specimens: a) M2-R0, b) M2-R15, c) M2-R30, d) M2-R45, e) M2-R60, f) Comparison of average values.

UPV increased as the GGBS content in the mix increased, in line with f_c. Comparing mixes M1-M3 with M4-M6, SF addition by 10 % of binder content caused a reduction in UPV. This reduction was more pronounced for M2 in which SF caused the UPV to drop by 22.3 % from 4465 (M2) to 3470 m/s (M5). The UPV results for the cubes up to 90 days are illustrated in Fig. 8(h) and Fig. 8(i) for M1-M3 and M4-M6 specimens, respectively. Among the 6 mixes, M2 was the only mix that showed increased UPV over the 90-day period. For instance, the UPV for mix M2 increased by 2.9 % from 7 to 28 days, and by 0.85 % from 28 to 90 days. Mixes M3, M5 and M6 showed an increase in UPV from 7 to 28 days, but a decline from 28 to 90 days. Mixes M1 and M4 showed a decline in UPV throughout the testing period, albeit at a higher rate from 7 to 28 days. This observed reduction in UPV throughout the testing period is due to the reduced formation of hydration products with time accompanied by the continuous formation of shrinkage microcracks as the specimens harden.

In light of the above, mix M2 which attained a 28-day cylinder f_c of slightly over 60 MPa and a slump>200 mm was chosen as the optimal mix design to investigate the effect of CR addition as replacement of NA in AAC. Mix M2 also showed the highest 28-day E_c, a stable increase in f_c and UPV over the testing period (90 days) with no signs of efflorescence.

4. Assessment of rubberised one-part AAC

4.1. Fresh and physical properties

The concrete slump results of the one-part RuAAC mixes are shown in Fig. 7(b), indicating a reduction in slump with an increase in CR replacement of NA. The slump of mix M2-R0 was 249 mm, dropping to 219 and 165 mm when 30 and 60 % of NA were replaced by CR particles, respectively. The reduction in concrete slump with an increase in CR replacement of NA was observed in several RuAAC studies [56,78] and RuC studies [48,49], and can be attributed to: a) the lower specific gravity of CR particles in comparison to NA, causing the fresh mix to flow less under its own self-weight with an increase in CR replacement, and b) CR particles have rough surfaces causing higher inter-particle friction. The rubberised mixes considered here achieved consistency classes S4 (>150 mm) and S5 (>210 mm), following BS 8500 [79], and no signs of segregation or bleeding were observed.

As shown in Fig. 11(a), the lower specific gravity of CR particles compared to that of NA caused a proportional reduction in concrete ρ with increasing ρ_{vr}. For instance, the density of the rubberised mixes at 28 days –determined from cylinders – dropped by 3.5, 8.6, 13.3 and

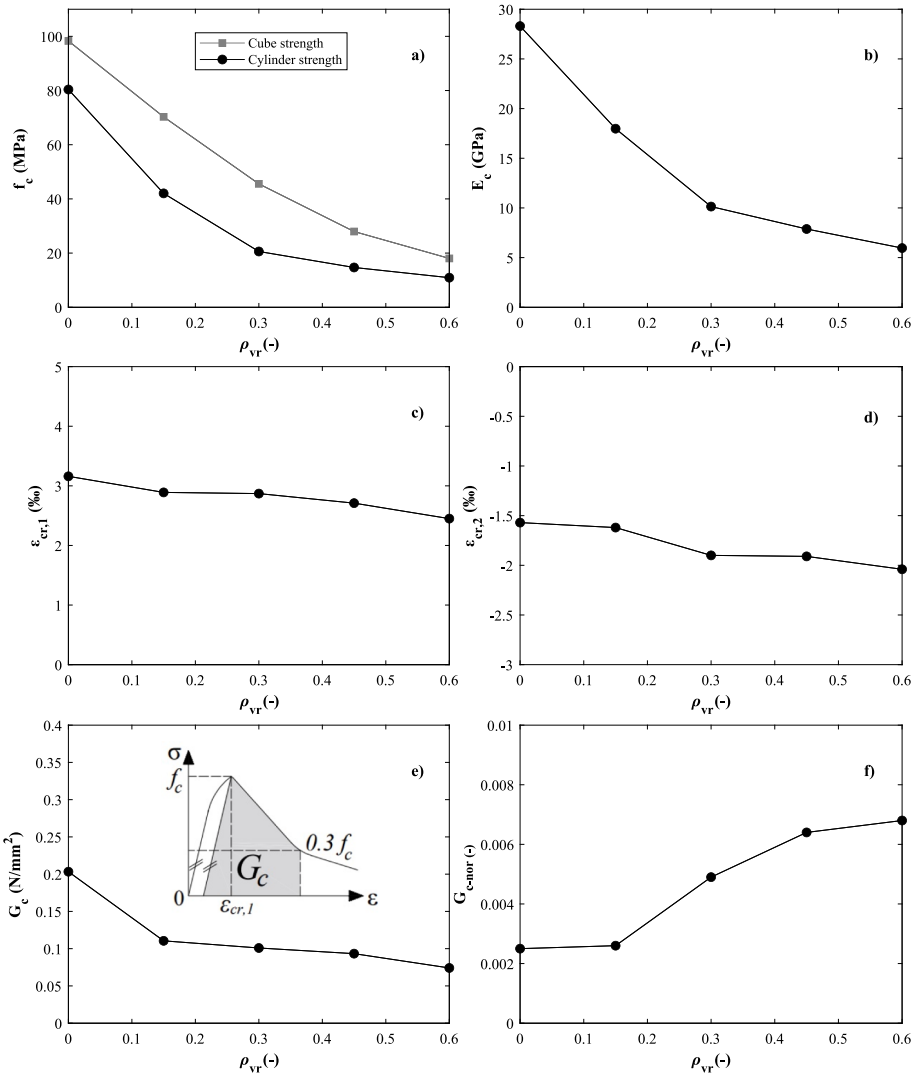


Fig. 13. Effect of ρ_{vr} on the mechanical properties: a) f_c, b) E_c, c) $\varepsilon_{cr,1}$, d) $\varepsilon_{cr,2}$, e) G_c, f) $G_{c\text{-nor}}$.

18.2 % for 15, 30, 45 and 60 % CR replacement of total NA, respectively, compared to the reference mix (M2-R0). The reduction in ρ with the increase in ρ_{vr} can also be observed for the cubes regardless of the curing age (Fig. 11(b)). Besides the lower specific gravity of rubber particles, the likelihood of CR particles to entrap air during mixing due to their serrated surfaces also contributes to the reduction in ρ [55].

The change in ρ of the cube specimens for a given mix over the 90 days was within ± 2.5 %. All the rubberised specimens showed a drop in ρ from 7 to 28 days, while the reference mix showed a slight increase in density of 0.7 % over the same period. The largest drop in ρ for the rubberised specimens from 7 to 28 days was observed for M2-R45 (2.2 %). From 28 to 90 days, the ρ of mixes M2-R15, M2-R30 and M2-R45 experienced a slight increase, while that of M2-R60 showed a slight reduction of about 0.5 %. The reference mix experienced a slight reduction in density from 28 to 90 days of nearly 0.7 %. Comparing the 7-day and 90-day ρ results, except for M2-R15 all mixes experienced a slight reduction, which is likely due to water evaporation and hardening. Mixes M2-R45 and M2-R60 have densities less than 2000 kg/m^3, and as such can be classified as lightweight concrete following BS 8500 [79].

4.2. Compressive strength

Fig. 11(c) illustrates the 28-day f_c of the rubberised mixes obtained from cylinder tests. The reference mix had a 28-day f_c of 80.4 MPa which dropped to 42.0, 20.6, 14.7 and 10.9 MPa for 15, 30, 45 and 60 % CR replacement of NA, respectively. This corresponded to a drop in f_c of around 47.7, 74.4, 81.7 and 86.4 %, respectively, when compared to the reference mix. The drop in f_c was more severe at lower ρ_{vr}, which is in agreement with previous studies [55]. The reduction in f_c due to an increase in CR replacement can be attributed to: a) the lower stiffness of rubber particles causing stress concentrations around them and the subsequent formation of microcracks, b) the formation of a weak interfacial transition zone (ITZ) between CR particles and the concrete matrix due to the hydrophobic property of rubber, and c) the tendency of CR particles to entrap air during mixing due to their serrated surfaces which increases the overall porosity.

The strength development of the one-part RuAAC mixes – determined from the cube specimens – is depicted in Fig. 11(d). All mixes experienced an increase in strength over the 90-day period indicating a stable formation of strength giving C-A—S—H and *N*-A—S—H gels. The reference mix (M2-R0) recorded the highest strength development gradient among the one-part RuAAC mixes of nearly 32.5 % from 7 to 28 days. Within the same period, the strength development gradient of the rubberised mixes generally decreased with the increase in ρ_{vr}. However, this was not the case from 28 to 90 days where the rubberised mixes exhibited higher strength development than that of the reference mix. The highest strength development within this period was observed

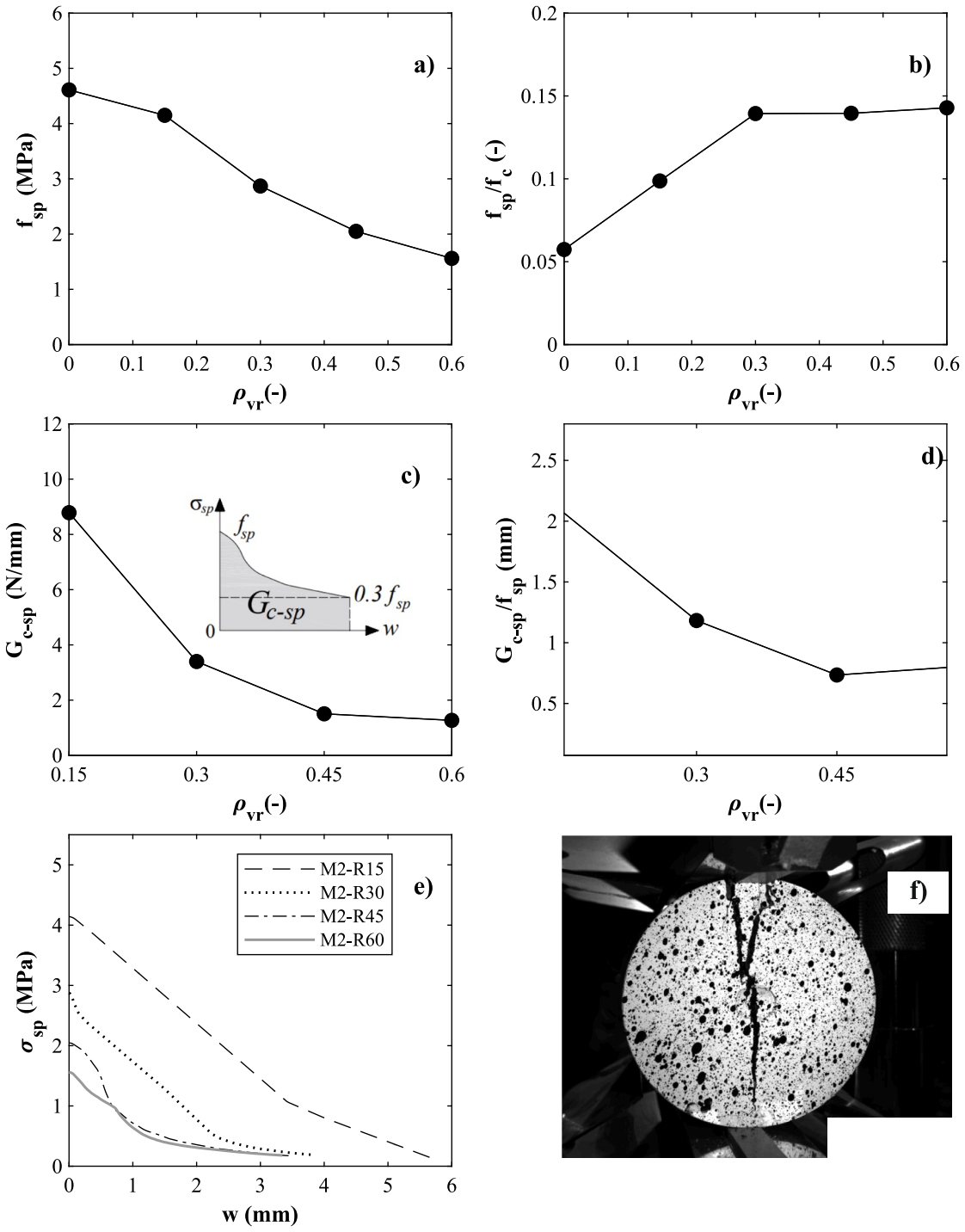


Fig. 14. Effect of ρ_{vr} on splitting strength properties: a) f_{sp}, b) f_{sp}/f_c, c) $G_{c\text{-}sp}$, d) $G_{c\text{-}sp}/f_{sp}$; e) average values splitting tensile stress vs crack width obtained from three tests; f) representative splitting failure of one-part RuAAC cylinders (image of M2-R60).

in M2-R30 (18.1 %), while the increase in $f_{c,cube}$ for the reference mix was only 5.4 %.

The 7- and 28-day strengths of the reference mix (M2-R0) were higher than that of M2 (in the previous section) despite having the same mix design. This was likely due to the higher ambient curing temperatures of M2-R0 which were cast during the summer. It is well known that AAMs are sensitive to the curing environment and higher surrounding temperatures result in higher f_c [10]. The 90-day strengths of M2 and M2-R0 were very similar (102.5 and 103.6 MPa, respectively), with higher strength development observed for M2 between 28 and 90 days, also due to the warmer ambient curing temperatures.

4.3. Stress–strain response

The stress–strain (σ-ε) response of the reference and RuAAC mixes is shown in Fig. 12 with average values depicted by black lines. A summary of the mechanical properties is shown in Fig. 13 and Table 4. In line with f_c, the stiffness of the rubberised mixes dropped with the increase in ρ_{vr}. This drop in E_c appears to be more severe when $\rho_{vr} \leq 30$ % and reduces for 30 % $< \rho_{vr} \leq$ 60 %. The reduction in E_c agrees with previous studies [57,59] and can be attributed to the lower stiffness of CR particles as compared to NA, causing a reduction in the stiffness of the RuAAC matrix. Additionally, as illustrated in Fig. 13(c) and Fig. 13(d), a

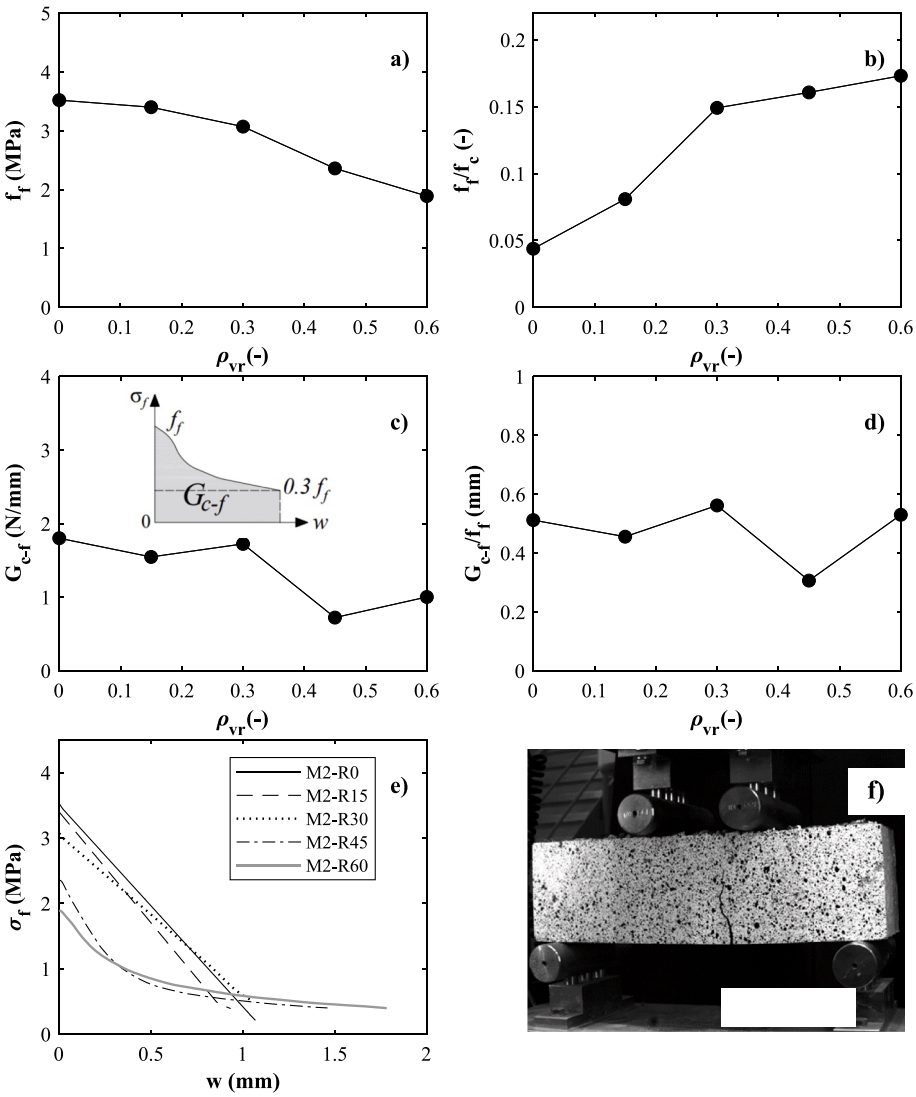


Fig. 15. Effect of ρ_{vr} on flexural strength properties: a) f_f, b) f_f/f_c, c) G_{c-f}, d) G_{c-f}/f_f; e) average flexural stress vs crack width curves obtained from three tests; f) representative flexural failure for one-part RuAAC prisms (image of M2-R60).

relatively high ρ_{vr} resulted in marginally lower $\varepsilon_{cr,1}$ and a slightly larger $\varepsilon_{cr,2}$, respectively. This effect was also noted for RuC [48,80,81], and can be mainly attributed to the drop in f_c. A higher ρ_{vr} also caused the axial descending branch of the σ-ε response to experience increased softening – a sign of gradual failure – as compared to the sharply linear and brittle descending branch of M2-R0. As depicted in Fig. 12(f), the lateral descending branch of the σ-ε curve became flatter with a higher ρ_{vr}.

Fig. 13(e) depicts G_c of the reference and rubberised mixes determined as the area under the σ-ε curve as shown in the diagram in the same figure. A higher CR replacement of NA caused G_c to drop in larger increments for low rubber contents (from M2-R0 to M2-R15) and more gradual for larger ρ_{vr} (from M2-R15 to M2-R60). This drop in G_c is due to the significantly higher f_c of M2-R0 compared to the rubberised mixes, and the gradual reduction in f_c with the increase in ρ_{vr}. The normalised crushing energy, $G_{c\text{-}nor}$, taken as G_c/f_c, is shown in Fig. 13(f). $G_{c\text{-}nor}$ was higher by a factor of 1.96 and 2.72, for mixes with 30 and 60 % CR, respectively, when compared to the reference mix (M2-R0). This shows that in normalised terms (i.e., for the same f_c), the addition of CR particles causes greater energy dissipation.

4.4. Splitting and flexural strength

The splitting tensile strength, f_{sp}, of the reference and rubberised mixes at 28 days is illustrated in Fig. 14(a), where it is evident that f_{sp} reduces with higher ρ_{vr}. The reduction in f_{sp} was 37.7 and 66.2 % for mixes with 30 and 60 % CR, respectively, compared to the reference. This reduction is mainly attributed to the lower stiffness of CR particles and the hydrophobic property of rubber causing a weaker ITZ between CR particles and the concrete matrix. The reduction in f_{sp} with higher ρ_{vr} was also observed for RuC [48] and conventional RuAAC [63,82]. Fig. 14(b) shows the ratio of f_{sp} to f_c which increases with higher ρ_{vr}. The change in f_{sp}/f_c was more pronounced with an increase in CR replacement up to $\rho_{vr} = 30$ %, and then more negligible afterwards.

The average splitting tensile stress - crack width ($\sigma_{sp} - w$) results are depicted in Fig. 14(e). The results for $\rho_{vr} = 0$ % are not shown, as upon reaching f_{sp} the specimen failed by a sudden splitting crack through the centre hence preventing the measurement of w. Meanwhile, the rubberised mixes remained intact even after reaching f_{sp}. Mixes with $\rho_{vr} \leq 30$ % experienced a rapid drop in σ_{sp} with greater cack opening as indicated by the straight lines in Fig. 14(e). On the other hand, mixes with $\rho_{vr} > 30$ % had a gradual drop in σ_{sp} accompanied by gradual crack opening. The energy dissipation under splitting tensile loading, $G_{c\text{-}sp}$, was calculated as shown in Fig. 14(c). A higher ρ_{vr} resulted in a larger drop in $G_{c\text{-}sp}$, with this being more severe at low rubber replacement ratios. For example, $G_{c\text{-}sp}$ for M2-15, M2-R30 and M2-R60 was 8.8, 3.4 and 1.3 N/mm, respectively, indicating a drop of 61.4 and 85.2 % for

Table 5
Summary of RuC data points.

Ref.	n_{mixes} [a] (-)	$f_{c,0}$ (MPa)	$\rho_{vr,min}$ (-)	$\rho_{vr,max}$ (-)
Replacement of FNA + CNA				
Fattuhi and Clark [93]	2	37.4	0.403	0.403
Khatib and Bayomy [94]	8	38.0	0.025	0.500
Guneyisi et al. [95]	60	53.8–85.7	0.025	0.500
Hernandez-Olivaresa and Barluenga [96]	3	93.4	0.030	0.080
Atahan and Sevim [97]	5	36.5	0.200	1.000
Xue and Shinozuka [98]	8	38.1	0.050	0.200
Naito et al. [99]	3	46.8	0.100	0.300
Su et al. [100]	4	61.1	0.072	0.082
Bompa et al. [48]	3	70.2	0.200	0.600
Total (FNA + CNA)	96			
Replacement of FNA				
Eldin and Senouci [101]	4	33.9	0.090	0.360
Topcu [102]	3	23.5	0.052	0.156
Khatib and Bayomy [94]	8	38.0	0.022	0.434
Cairns et al. [103]	3	49.3	0.050	0.250
Ghaly and Cahill [104]	9	12.6–30.1	0.081	0.256
Bignozzi and Sandrolini [105]	2	33.0	0.137	0.205
Taha et al. [106]	4	26.3	0.088	0.352
Aiello and Leuzzi [107]	4	27.1	0.023	0.112
Azevedo et al. [108]	9	71.1	0.028	0.153
Liu et al. [109]	3	43.4	0.015	0.045
Raffoul et al. [49]	5	61.7	0.045	0.600
Total (FNA)	54			
Replacement of CNA				
Eldin and Senouci [101]	4	33.5	0.160	0.640
Topcu [102]	3	23.5	0.098	0.294
Toutanji et al. [110]	4	31.9	0.150	0.600
Khatib and Bayomy [94]	8	38.0	0.028	0.566
Hernandez-Olivares et al. [111]	1	40.0	0.035	0.035
Cairns et al. [103]	3	49.3	0.050	0.250
Taha et al. [106]	4	26.3	0.162	0.648
Turatsinze and Garros [112]	4	42.4	0.102	0.254
Zheng et al. [113]	3	53.8	0.096	0.289
Aiello and Leuzzi [107]	3	45.8	0.062	0.188
Ganjian et al. [114]	3	32.5	0.024	0.049
Bing and Ning [115]	8	39.0–61.0	0.156	0.622
Total (CNA)	48			

[a] *number of rubberised mixes (not including the reference mixes).*

Table 6
Summary of RuAAC data points.

Ref.	n_{mixes} [a] (-)	$f_{c,0}$ (MPa)	$\rho_{vr,min}$ (-)	$\rho_{vr,max}$ (-)
Replacement of FNA + CAN				
This study[b]	4	80.4	0.150	0.600
Aly et al. [63]	2	37.4	0.200	0.300
Aslani et al. [82]	2	42.1	0.045	0.090
Pham et al. [58]	2	54	0.150	0.300
Total (FNA + CAN)	10			
Replacement of FNA				
Park et al. [60]	7	28.6–42.5	0.013	0.050
Azmi et al. [116]	4	65.0	0.050	0.200
Long et al. [78]	3	58.0	0.200	0.600
Azmi et al. [117]	4	67.0	0.050	0.200
Zaetang et al. [118]	4	37.4	0.250	1.000
Ali et al. [119]	2	15.5	0.080	0.120
Rajaei et al. [59]	3	40.6	0.200	0.600
Abdelmonim and Bompa [62][b]	9	50.6	0.100	0.300
Total (FNA)	36			
Replacement of CAN				
Dong et al. [57]	2	58.0	0.104	0.207
Total (CAN)	2			

[a] *number of rubberised mixes (not including the reference mixes).*
[b] *one-part RuAAC.*

M2-R30 and M2-R60, respectively, when compared to M2-R15. This reduction in $G_{c\text{-}sp}$ is due to the lower f_{sp} with higher ρ_{vr} and the larger crack openings that are seen with lower ρ_{vr}. Dividing $G_{c\text{-}sp}$ by f_{sp} (i.e., normalised terms) does not show much of a difference with $G_{c\text{-}sp}/f_{sp}$ ratio reducing with higher ρ_{vr} up to 45 % and then increasing slightly for $\rho_{vr} =$ 60 %. This means that despite the more gradual failure with higher ρ_{vr}, $G_{c\text{-}sp}$ still reduces even when normalised values are considered. The rubberised specimens remained intact after failure with the formation of few splitting cracks, often joining together, indicating a more ductile and gradual failure as shown in Fig. 14(f) for M2-R60.

The 28-day flexural strength, f_f, of the rubberised mixes followed the same trend observed for f_c and f_{sp} and the results are illustrated in Fig. 15 (a). Compared with the reference mix, the drop in f_f due to 15, 30, 45 and 60 % CR replacement of NA was 3.4, 12.8, 33 and 46.3 %, respectively. The reduction in f_f with ρ_{vr} is in agreement with the literature for conventional two-part RuAAC [59,63]. The ratio of f_f/f_c increases with ρ_{vr}, being 4.4, 14.9, and 17.3 % for M2-R0, M2-R30 and M2-R60, respectively. Again, the increase in f_f/f_c was more significant for $\rho_{vr} \leq$ 30 % as shown in Fig. 15(b). The flexural stress – crack width ($\sigma_f - w$) curves (Fig. 15(e)) agreed with those of the splitting tensile loading conditions, indicating a rapid drop in σ_f after reaching f_f for $\rho_{vr} \leq 30$ %, and a more gradual reduction in σ_f for $\rho_{vr} > 30$ %. The energy dissipation under flexural loading, $G_{c\text{-}f}$ – calculated as shown in Fig. 15(c) – depended on ρ_{vr} but was almost unaffected up to $\rho_{vr} = 30$ %, and then dropped for $\rho_{vr} \geq 45$ %. Looking at $G_{c\text{-}f}/f_f$ (Fig. 15(d)) further shows that the addition of rubber did not have a consistent effect. The highest and lowest $G_{c\text{-}f}/f_f$ ratios were observed in M2-R30 and M2-R45, which were 9.7 % higher and 40.2 % lower than that of M2-R0, respectively. All prisms failed through a single crack within the constant moment region (i.e., between the points of load application) as shown for M2-R60 in Fig. 15(f).

4.5. Ultrasonic pulse velocity

The UPV of the concrete cylinders at 28 days is shown in Fig. 11(e). Much like the ρ and f_c results, the UPV dropped with the increase in CR replacement of NA indicating the presence of more voids for high CR replacement. The reference mix had a UPV value of 4693 m/s, and this was lower by 20.8 and 40.1 % for mixes with 30 and 60 % CR replacement, respectively. Fig. 11(f) depicts the UPV results for the cube specimens of the one-part RuAAC mixes up to 90 days. The UPV results for the reference mix increased over 90 days, with a higher rate of increase from 7 to 28 days (0.9 %), followed by a slower rate of increase from 28 to 90 days (0.3 %). The rubberised mixes did not show a clear pattern over the 90 days period, but the change in UPV was minimal (i.e., within ± 2 %). Except for M2-R0, the recorded UPV values from the concrete cylinders were lower than that of the concrete cubes. Furthermore, the reduction in UPV with the increase in ρ_{vr} was higher for the concrete cylinders than that for the concrete cubes. The average reduction in UPV over the 90 days period – as determined from the cube specimens – was 4, 8.5, 16.9 and 22.8 % for ρ_{vr} values of 15, 30, 45 and 60 %, respectively, when compared to the reference mix.

5. Analytical expressions and constitutive models

Analytical expressions and constitutive models to predict the mechanical properties of one-part RuAAC are presented in this section. An extensive database of 241 RuC mixes (Table 5) and 57 RuAAC mixes (Table 6) corresponding to 723 RuC and 171 RuAAC samples, respectively, available in the literature was assembled to allow direct comparison with the results of this study and to validate the analytical expressions proposed.

5.1. Compressive strength

The compressive strengths in Table 5 and Table 6 were determined

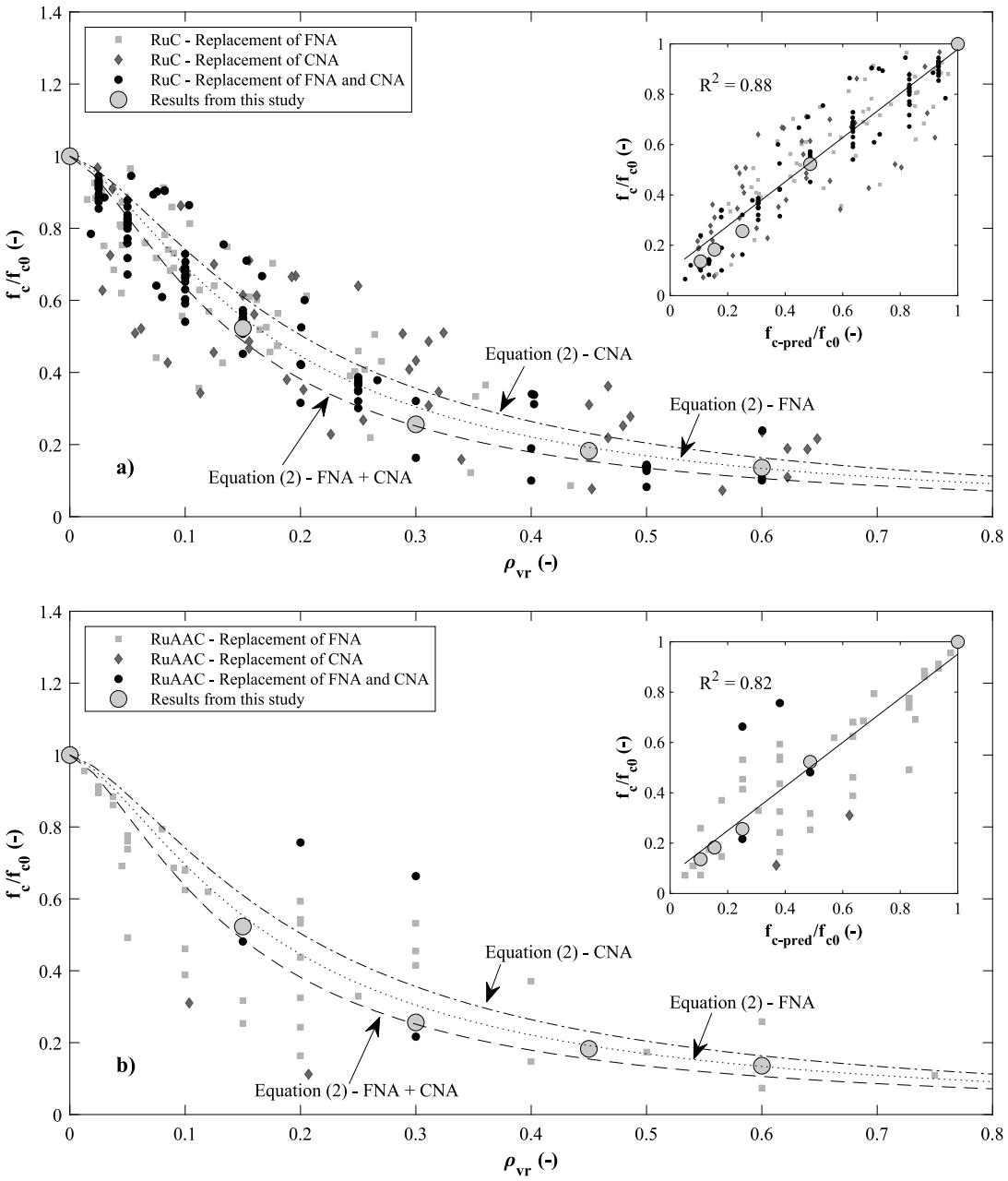


Fig. 16. Compressive strength degradation as a function of ρ_{vr}: a) comparison with RuC, b) comparison with RuAAC.

from concrete cylinders and cubes of various sizes, indicating that the f_c is size and aspect ratio dependent. For example, the volumetric expansion of cylinders is different from that of cubes made of the same material resulting in different f_c. To account for the shape effect of concrete specimens, Nielsen and Hoang [83] proposed an expression relating the compressive strength, $f_{c(d)}$, and volume, $V_{c(d)}$, of a given specimen to that of the strength of a reference mix, $f_{c,ref}$, with a specific volume, $V_{c,ref}$, as given by Eq. (1). As such, to allow for a direct comparison of the results in Table 5 and Table 6 with those from this study, the compressive strengths were normalised to a ϕ100 × 200 mm size cylinder.

$$f_{c,ref} = f_{c(d)}\left(V_{c(d)}/V_{c,ref}\right)^{1/30} \quad (1)$$

Fig. 16(a) and (b) depict the f_c degradation curve with the increase in ρ_{vr} for RuC and RuAAC, respectively, both for the results from this study and the literature. The large scatter in the results is attributed to different CR sizes replacing NA, water-to-cement ratios, types of natural mineral aggregates, and admixtures used. Moreover, for RuAAC, the scatter could be due to different precursors and alkaline solutions used, as well as different curing conditions. It is worth noting that the results from this study for one-part RuAAC fall within the scatter of both RuC and RuAAC results, indicating that the mechanism governing the strength degradation of RuC, two-part RuAAC and one-part RuAAC, with increasing ρ_{vr}, is the same.

The ρ_{vr}-dependent f_c can be estimated using Eq. (2a) introduced previously for RuC by the authors [48]. The factor λ in Eq. (2a) depends on the type of NA replaced (λ = 2.9 in this study for the replacement of CR particles with both FNA and CNA). The parameter f_{c0} is the strength of the reference mix with $\rho_{vr} = 0$, and $f_{c\text{-}pred}$ in Fig. 16 is the predicted compressive strength.

As shown in Fig. 16(a) and Fig. 16(b), Eq. (2) captures the reduction in f_c reasonably well for one-part RuAAC, RuC and two-part RuAAC. Based on the one-part RuAAC results in this study, the average test-to-predicted f_c using Eq. (2a) was 1.11 with a coefficient of variation (COV) of 9.55 %. Excellent correlation between the test and predicted

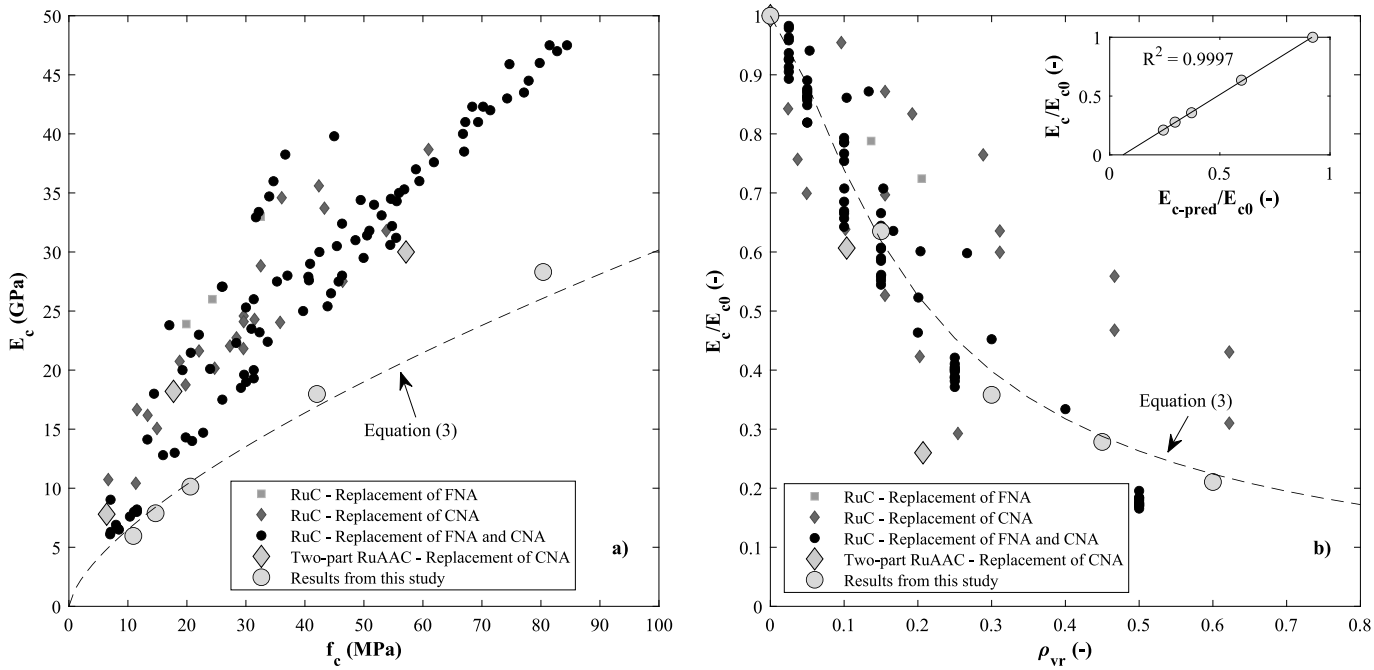


Fig. 17. Modulus of elasticity results: a) E_c, vs f_c, b) degradation of E_c as a function of ρ_{vr}.

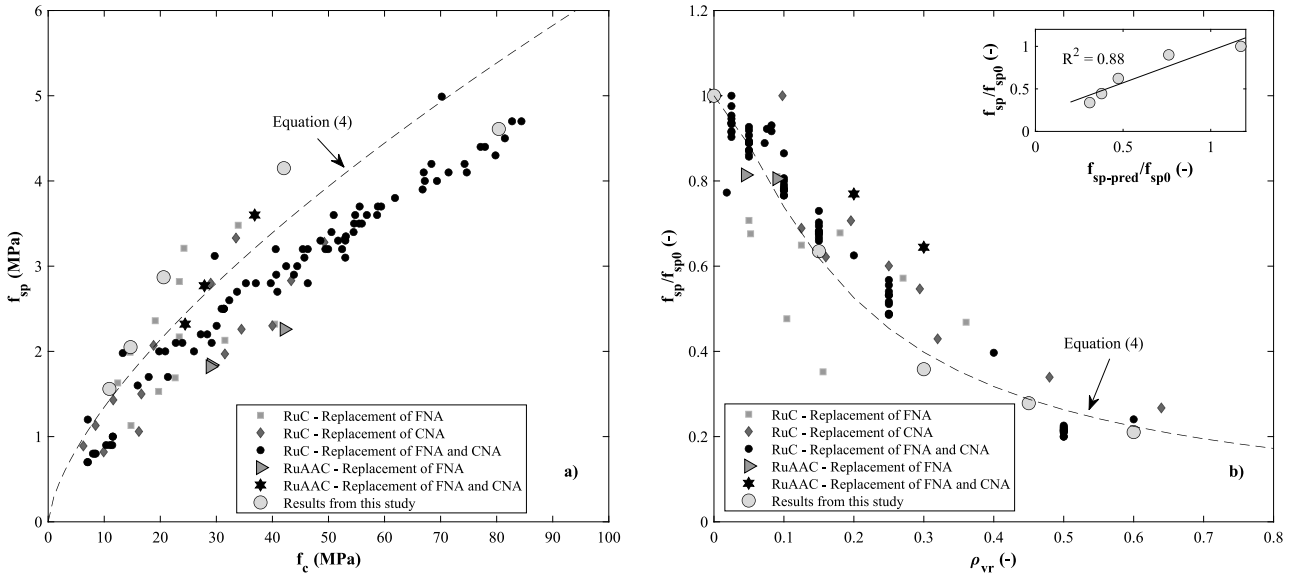


Fig. 18. Splitting tensile strength results: a) f_{sp} vs f_c, b) degradation of f_{sp} as a function of ρ_{vr}.

values is reported when COV is less than 12 %, while fair and poor correlations are assumed when COV is less than 18 % and>25 %, respectively [48].

$$\frac{f_c}{f_{c0}} = \frac{1}{1+2\left(\frac{3\lambda\rho_{vr}}{2}\right)^{3/2}} \rightarrow 0 \le \rho_{vr} \le 0.6 \tag{2a}$$

$$\lambda = \begin{cases} 2.90 \rightarrow replacementofFNAandCNA \\ 2.43 \rightarrow replacementofFNA(\le 5mm) \\ 2.08 \rightarrow replacementofCNA(> 5mm) \end{cases} \tag{2b}$$

5.2. Modulus of elasticity

The available E_c results from the studies presented in Table 5 and Table 6, together with the results for one-part RuAAC from this investigation, are plotted against their corresponding f_c in Fig. 17(a). This includes the data points from 114 RuC mixes and 3 two-part RuAAC mixes. It is shown that there is a direct relationship between E_c and f_c. For the one-part RuAAC mixes, E_c was notably less than for RuC with the same f_c. It was reported previously that AAC material typically develops lower stiffness than that of OPC-based CCM [84,85]. This could mean that strength giving gels, including both C-A—S—H and *N*-A—S—H gels, in AAMs lead to lower stiffness than that of the C—S—H gel developed from OPC hydration. Based on the results from this study, E_c for one-part RuAAC can be predicted with good accuracy as a function of f_c using Eq. (3), with an average test-to-predicted value of 0.98 and a COV of 8.27 %.

$$E_c = 6500\left(\frac{f_c}{10}\right)^{2/3} \tag{3}$$

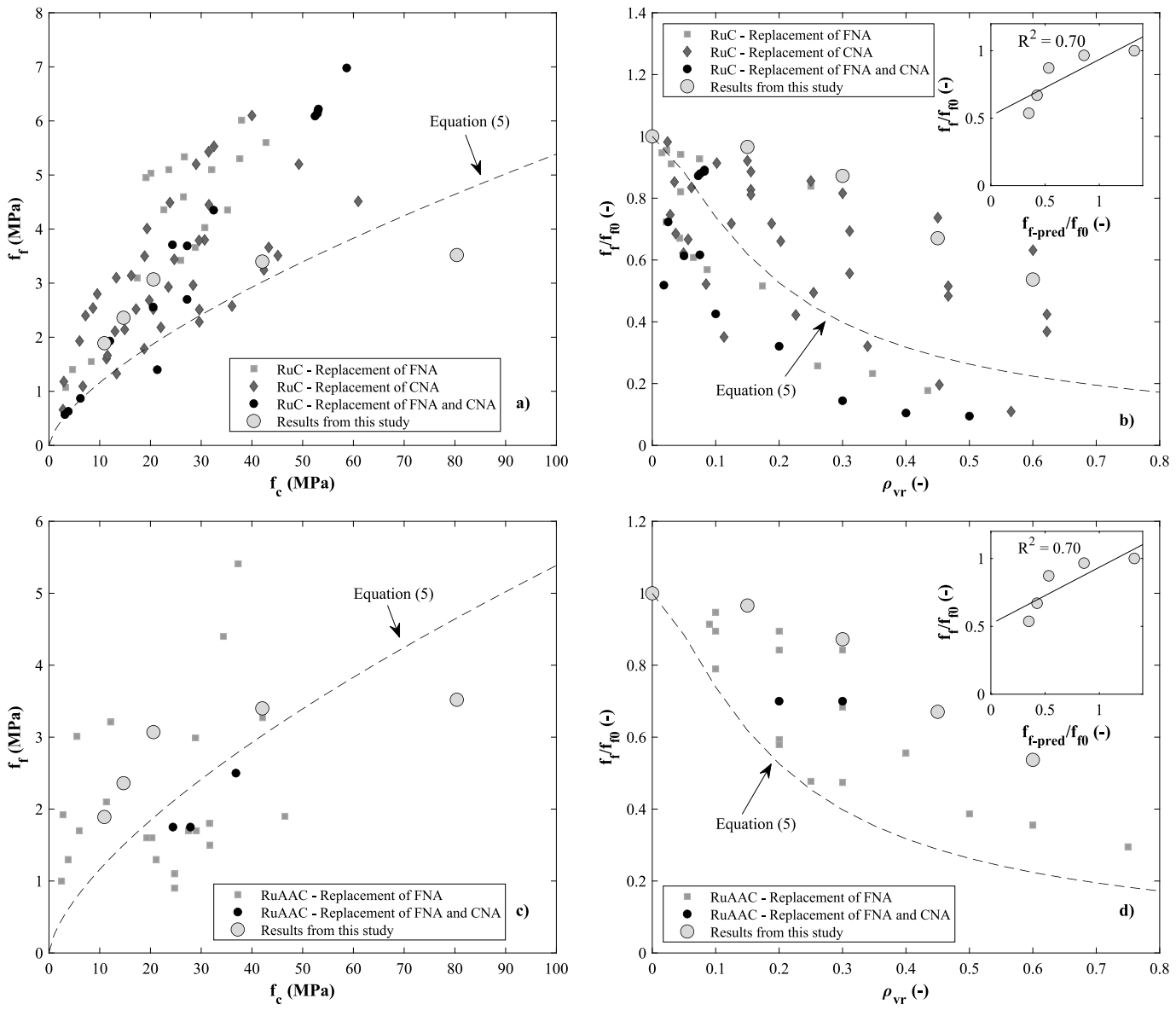


Fig. 19. Flexural strength results: a) RuC f_f vs f_c, b) RuC degradation of f_f as a function of ρ_{vr}, c) RuAAC f_f vs f_c, d) RuAAC degradation of f_f as a function of ρ_{vr}.

Fig. 17(b) illustrates the degradation in E_c with increasing CR replacement of NA. E_{c0} and $E_{c\text{-}pred}$ in Fig. 17(b) denote the elastic modulus of the reference mix and predicted elastic modulus, respectively. The stiffness of concrete materials reduces with the increase in ρ_{vr}, without notable difference in the degradation mechanism for different concrete materials (i.e., RuC and one-part RuAAC). Much like the compressive strength results, the stiffness results from this study largely fall within the scatter of RuC data points.

5.3. Splitting tensile strength

Fig. 18(a) illustrates the relationship between f_{sp} and f_c based on the available data from Table 5 and Table 6. This includes 106 RuC mixes, 6 two-part RuAAC mixes and the results from this investigation. Clearly, f_{sp} increases proportionally with f_c, although the results from this study seem to show a higher increase in f_{sp} for a given f_c in comparison to that of RuC. Based on the results in this study, f_{sp} of one-part RuAAC can be predicted using Eq. (4) as a function of f_c as shown in Fig. 18. Eq. (4) gives an average test-to-predicted value of 1.13 and a COV of 13.66 % for the one-part RuAAC mixes in this study. Fig. 18(b) depicts the degradation of f_{sp} with increasing ρ_{vr} where f_{sp0} stands for the splitting strength of the reference mix and $f_{sp\text{-}pred}$ represents the predicted splitting strength. The reduction in f_{sp} for one-part RuAAC falls within the scatter of RuC results indicating a similar mechanism controlling the drop in f_{sp} with increasing ρ_{vr}.

$$f_{sp} = 0.29 f_c^{2/3} \tag{4}$$

5.4. Flexural strength

The f_f results for one-part RuAAC in this study are plotted in Fig. 19 together with those available for RuC and RuAAC mixes. This includes a total of 73 RuC mixes and 24 RuAAC mixes. Comparing the relationship between f_f and f_c in Fig. 19(a) and Fig. 19(c), the f_f results of one-part RuAAC fall within the scatter of data for both RuC and RuAAC when f_c is less than 50 MPa. However, for the reference one-part AAC mix (ρ_{vr} = 0), f_f was significantly lower than the overall trend for RuC and RuAAC data. The flexural strength for one-part RuAAC can be estimated with Eq. (5), giving an average test-to-predicted value of 1.33 and COV of 25.4 %.

$$f_f = 0.25 f_c^{2/3} \tag{5}$$

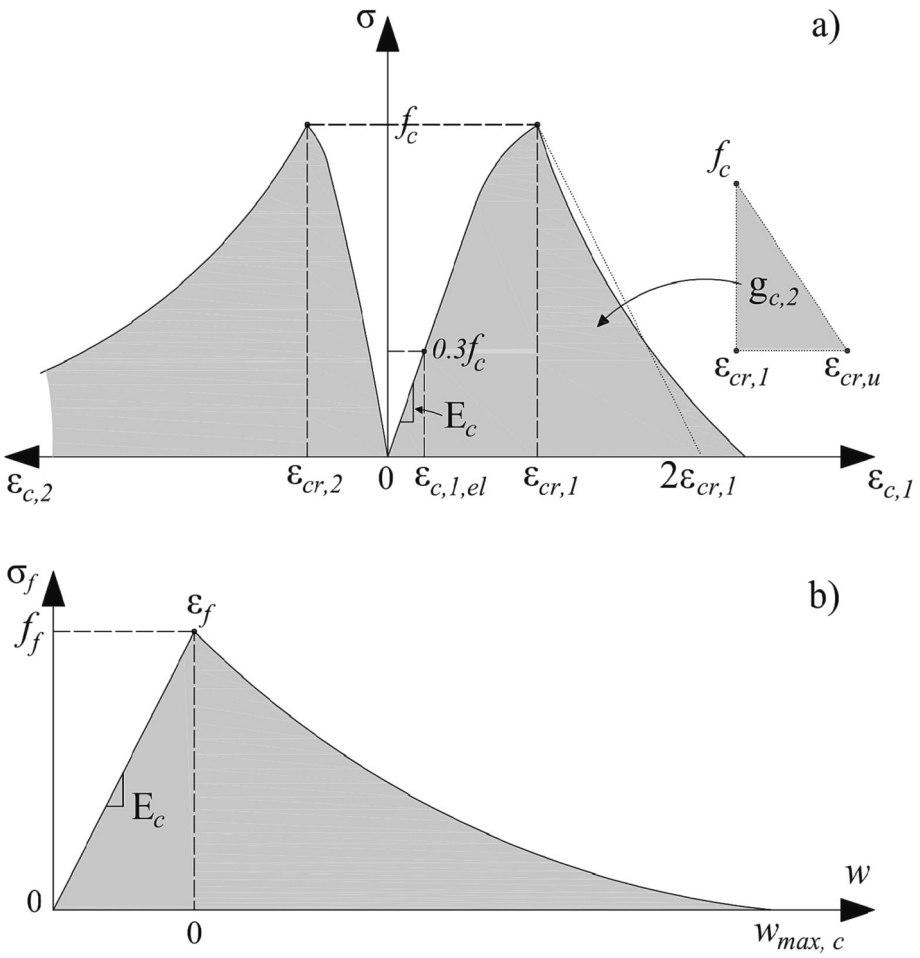


Fig. 20. Illustration of constitutive models: a) σ-ε, b) σ_f -w.

The degradation in f_f with the increase in ρ_{vr} is illustrated in Fig. 19 (b) and Fig. 19(d). The parameters f_{f0} and $f_{f\text{-}pred}$ in these figures denote the flexural strength of the reference mix and the predicted flexural strength, respectively. The reduction in f_f with the increase in CR replacement of NA for the one-part RuAAC mixes investigated in this study was more subtle with increasing ρ_{vr} and generally Eq. (5) and Eq. (2) provide conservative estimates for all ρ_{vr} ranges (Fig. 19(a) and (c)). The degradation of f_f with increasing ρ_{vr} for the one-part RuAAC was different from that observed for RuC and two-part RuAAC. However, due to the limited number of one-part RuAAC results in this investigation, further studies are needed to validate the scalar factors in Eq. (5) for one-part RuAAC.

5.5. Stress–strain response

The full σ-ε of concrete materials is essential when considering the nonlinear analysis of concrete members. Based on the results of this study, a constitutive model for the unconfined σ-ε response of one-part RuAAC is presented. The model is a modified version of a previous constitutive model for RuC developed by the authors [48]. The presented model uses the expressions proposed for f_c in Eq. (2) and E_c in Eq. (3). The axial crushing strain, $\varepsilon_{cr,1}$, is determined as a function of the crushing strain of the reference mix, $\varepsilon_{cr0,1}$, and ρ_{vr} from Eq. (6). Meanwhile, the lateral crushing strain, $\varepsilon_{cr,2}$, can be determined as a function of $\varepsilon_{cr,1}$ and ρ_{vr} from Eq. (7).

$$\frac{\varepsilon_{cr,1}}{\varepsilon_{cr0,1}} = (1-\rho_{vr})^{1/4} \rightarrow 0 \le \rho_{vr} \le 0.6 \tag{6}$$

$$\varepsilon_{cr,2} = \frac{1}{2(1-\rho_{vr})^{1/2}}\varepsilon_{cr,1} \rightarrow 0 \le \rho_{vr} \le 0.6 \tag{7}$$

The constitutive model for the axial σ-ε response is divided into three regions: a) initial elastic response, b) softening-ascending response prior to crushing, and c) softening-descending response after crushing. In the initial stage where the σ is less than $0.3f_c$, a perfectly elastic response following Hooke's law is assumed as given by Eq. (8). In the softening-ascending region prior to crushing, the response is represented by Eq. (9) which is a second-degree polynomial accounting for the formation of micro-cracks that cause the response to deviate slightly from a perfectly elastic case. After crushing, macro-cracks form and failure is controlled by sliding. This is represented by Eq. (10) which is also a second-degree polynomial function that is dependent on the post-crushing energy, $g_{c,2}$, represented by the triangular region in Fig. 20(a) and given in Eq. (12).

$$\sigma = E_c\varepsilon_{c,1} \rightarrow 0 \le \varepsilon_{c,1} \le \varepsilon_{c,1,el} = \frac{0.3f_c}{E_c} \tag{8}$$

$$\frac{\sigma}{f_c} = \frac{5}{3}\left(\frac{\varepsilon_{c,1}-\varepsilon_{c,1,el}}{\varepsilon_{cr,1}}\right) - \left(\frac{\varepsilon_{c,1}-\varepsilon_{c,1,el}}{\varepsilon_{cr,1}}\right)^2 + 0.3 \rightarrow \varepsilon_{c,1,el} \le \varepsilon_{c,1} \le \varepsilon_{cr,1} \tag{9}$$

$$\frac{\sigma}{f_c} = \frac{1}{8}\left(\frac{f_c}{g_{c,2}}-1\right)^2\left(\frac{\varepsilon_{c,1}-\varepsilon_{cr,1,}}{\varepsilon_{cr,1}}\right)^2 - \frac{5}{8}\left(\frac{f_c}{g_{c,2}}-1\right)\left(\frac{\varepsilon_{c,1}-\varepsilon_{cr,1,}}{\varepsilon_{cr,1}}\right) + \frac{f_{c,2}}{f_c} \rightarrow \varepsilon_{c,1} > \varepsilon_{cr,1} \tag{10}$$

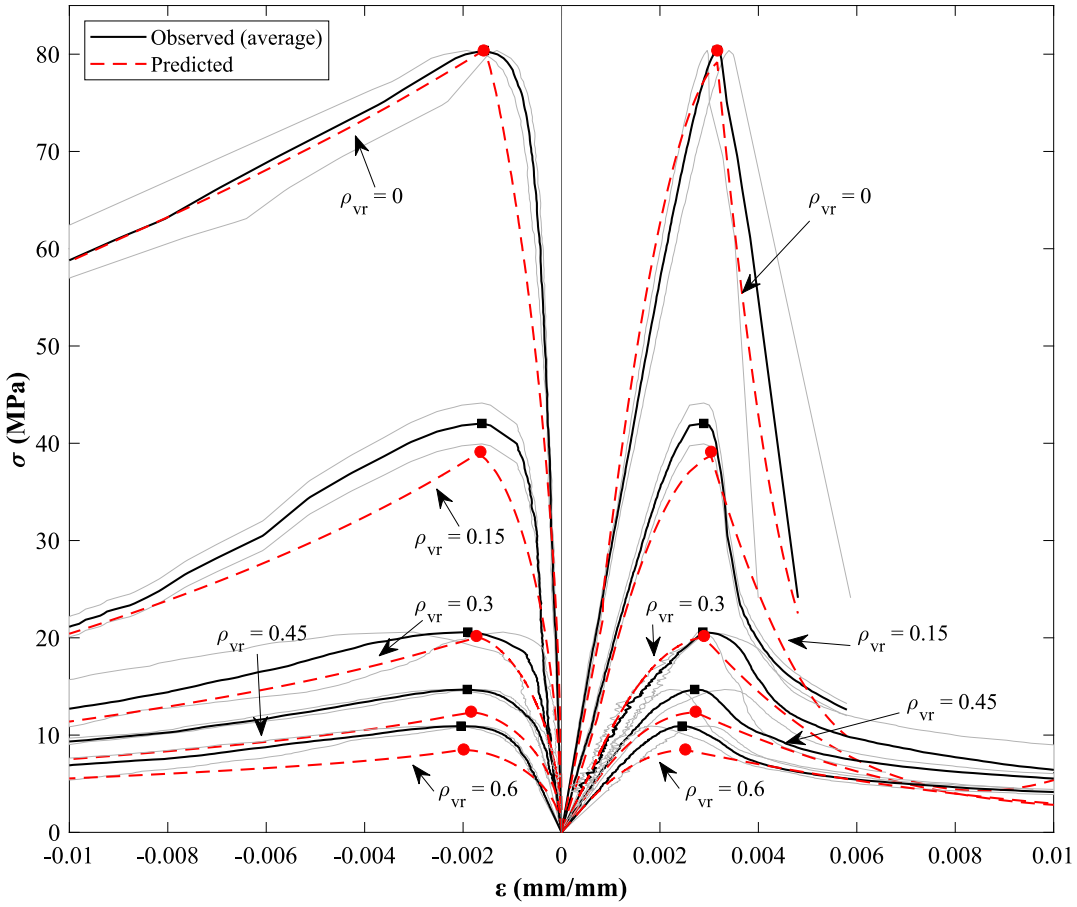


Fig. 21. Validation of unconfined σ-ε constitutive model.

$$\frac{f_{c,2}}{f_c} = \frac{5}{3}\left(\frac{\varepsilon_{cr,1} - \varepsilon_{c,1,el}}{\varepsilon_{cr,1}}\right) - \left(\frac{\varepsilon_{cr,1} - \varepsilon_{c,1,el}}{\varepsilon_{cr,1}}\right)^2 + 0.3 \tag{11}$$

$$g_{c,2} = [(1+\rho_{vr})f_c]^{2/3} \tag{12}$$

The lateral σ-ε response of one-part RuAAC can be predicted using Eqs. (13)-(15). The response is divided into two regions: a) pre-peak regime, and b) post-peak regime. The lateral strain, $\varepsilon_{c,2}$, in the pre-peak regime is a function of $\varepsilon_{c,1}$, σ/f_c, and ρ_{vr} and given by Eq. (13). Meanwhile, in post-peak regime, $\varepsilon_{c,2}$ is controlled by $\varepsilon_{c,1}$ and σ/f_c as shown in Eq. (14). The lateral σ-ε response requires the determination of the axial response using Eqs. (8)-(12) and $\varepsilon_{cr,2}$ in Eq. (7).

$$\frac{\varepsilon_{c,2}}{\varepsilon_{c,1}} = \left(\frac{\sigma}{f_c}\right)\frac{1}{2(1-\rho_{vr})^{1/2}} \rightarrow 0 \le \varepsilon_{c,1} < \varepsilon_{cr,1} \tag{13}$$

$$\frac{\varepsilon_{c,2}}{\varepsilon_{c,1}} = C\left(1 - \frac{\sigma}{f_c}\right) + \frac{\varepsilon_{cr,2}}{\varepsilon_{c,1}} \rightarrow \varepsilon_{c,1} > \varepsilon_{cr,1} \tag{14}$$

$$C = \begin{cases} 8 for \rho_{vr} = 0 \\ 4 for 0 < \rho_{vr} \le 0.6 \end{cases} \tag{15}$$

Validation of the unconfined σ-ε constitutive model presented here is given in Fig. 21. The shaded grey areas in the figure represent the range of maximum and minimum values as determined from the three identical cylindrical specimens, while the black and red-dotted lines represent the test average values and predicted results, respectively. The comparative assessment between observed and predicted constitutive response in Fig. 21 shows close agreement. The average test-to-predicted value for $\varepsilon_{cr,1}$, based on Eq. (6), was 0.98 with a COV of 1.8 %. As for $\varepsilon_{cr,2}$, the average test-to-predicted value was 1.05 with a COV of 3.56 %.

5.6. Flexural stress-crack width response

Flexural tests are commonly used to infer the direct tensile behaviour of concrete materials [86]. Using the σ_f-w results obtained in this study, a ρ_{vr} – dependent constitutive model is presented for the flexural response as given by Eqs. (16)-(20) and illustrated in Fig. 20(b).

$$\frac{\sigma_f}{f_f} = \frac{E_c\varepsilon}{f_f} \rightarrow \varepsilon < \varepsilon_f = \frac{f_f}{E_c} \tag{16}$$

$$\frac{\sigma_f}{f_f} = \frac{1}{1 + \alpha_w[\lambda_w(w/w_{max,c})]^{(2-\rho_{vr}^2)}} \rightarrow \varepsilon \ge \varepsilon_f \tag{17}$$

$$\alpha_w = 8(1+\rho_{vr}) - 7.5 \tag{18}$$

$$\lambda_w = 3(9\rho_{vr} + 1) \tag{19}$$

$$w_{max,c} = w_{max,0} + 2.5\rho_{vr}(5\rho_{vr} + 1) \tag{20}$$

The equations are based on a previous model by the authors for cementitious composites incorporating plastic particles [86]. An elastic response is assumed in the pre-peak region as given by Eq. (16), while an inverse power function is used to represent the response in the post-peak regime. The softening response given by Eq. (17) is a function of f_f, ρ_{vr} and ultimate crack displacement, $w_{max,c}$ (Fig. 20(b)). The latter is a function of both ρ_{vr} and the ultimate crack displacement of the reference mix, $w_{max,0}$. The value of $w_{max,0}$ used here was extrapolated from the results in this study. Validation of the σ_f-w constitutive model against the experimental results is shown in Fig. 22. The predicted response fits relatively well with the experimental results, being mostly within the experimental ranges shown by the grey area in Fig. 22.

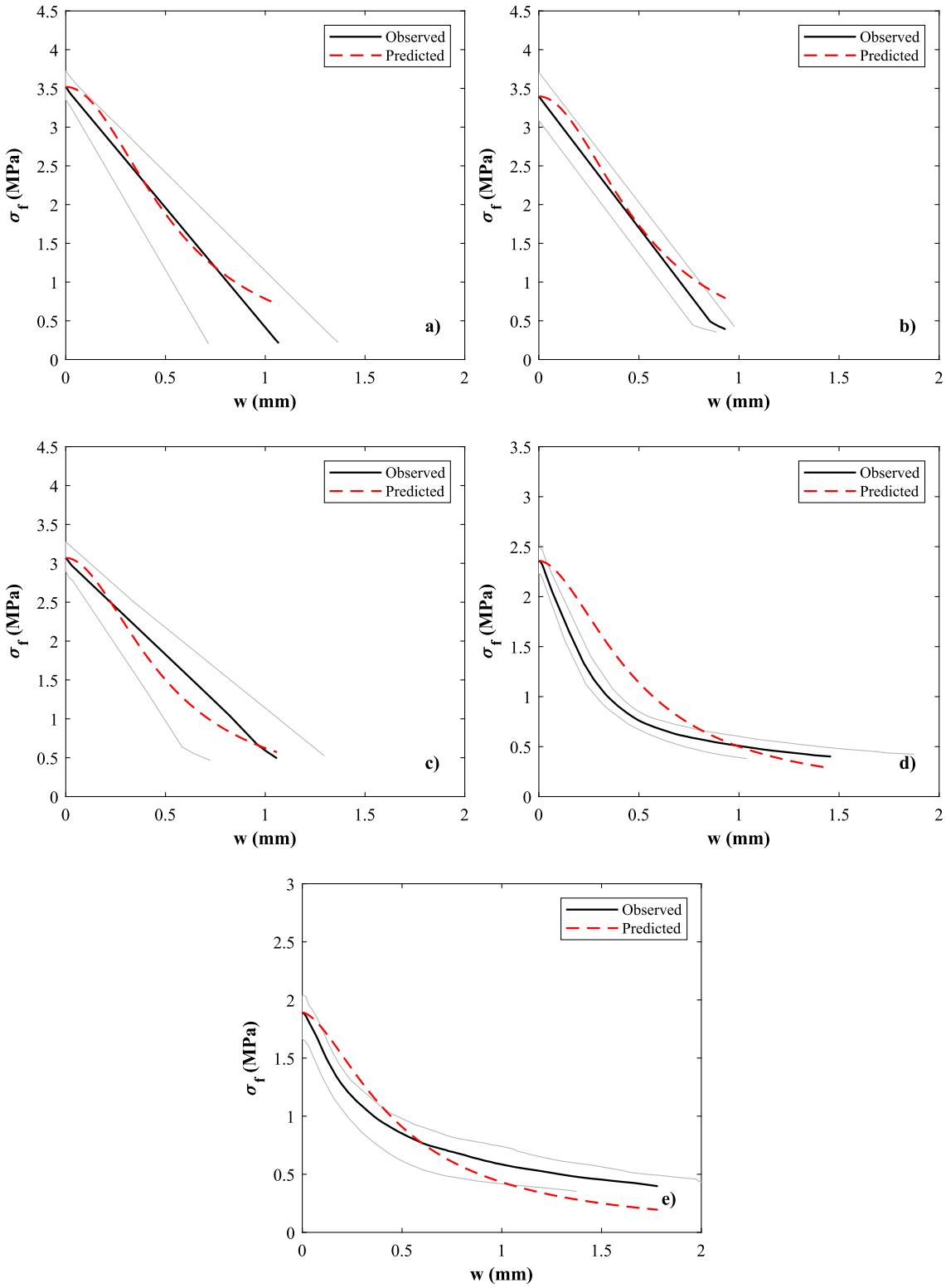


Fig. 22. Validation of σ_f -w constitutive model: a) M2-R0, b) M2-R15, c) M2-R30, d) M2-R45, e) M2-R60.

6. Conclusions

This study focused on assessing the mechanical properties of rubberised one-part alkali-activated concrete (one-part RuAAC), and on considering the optimal use of their constituent materials. Different precursor proportions, binder-to-aggregate ratios, Na_2SiO_3-anhydrous (activator) contents, and borax (solid admixture) dosages were investigated to obtain an optimal mix design. Crumb rubber (CR) particles from end-of-life tyres were then used to replace up to 60 vol% of the natural mineral aggregates. The effect of CR particles on the workability, elastic modulus, compressive, splitting tensile, and flexural strength, as well as complete constitutive response in compression and flexure, were investigated. In addition, a database of 241 rubberised concrete (RuC) mixes and 57 two-part RuAAC mixes was assembled to

enable direct comparisons with the results from this study, as well as to develop analytical expressions and constitutive models to predict the mechanical response of one-part RuAAC with varying CR ratios. From the findings, the following main remarks can be drawn:

- The results showed that an FA-to-GGBS ratio of 20:80, binder-to-aggregate ratio of 0.4, an activator-to-binder dosage of 12 %, and a borax-to-binder dosage of 5 % were the optimal mix proportions for ambient curing conditions considering both workability and compressive strength development up to 90 days.
- For FA and GGBS-based one-part AAC, a high GGBS content in the mix led to high f_c and a relatively low concrete slump. The addition of SF as a supplementary precursor by 10 % of total binder content led to a remarkable increase in concrete slump with varying effects on f_c. Mixes with both FA and GGBS showed a reduction in f_c with the addition of SF, while those with GGBS only showed an increase in f_c.
- The addition of 10 % SF to the FA- and GGBS-based one-part AAC mixes caused E_c to reduce and G_c to increase, albeit at a different rate depending on the FA-to-GGBS ratio. Moreover, mixes with SF showed small white deposits on the surface of the specimens at 90 days, indicating the occurrence of efflorescence.
- The replacement of natural mineral aggregates with CR particles caused f_c, E_c, $\varepsilon_{cr,1}$, f_{sp} and f_f to reduce. This reduction was a function of the CR replacement ratio of natural mineral aggregates. The post-peak axial σ-ε response became softer with an increase in ρ_{vr}, while $\varepsilon_{cr,2}$ increased slightly with the increase in CR replacement of natural mineral aggregates.
- No significant difference occurred in the degradation curves of f_c with the increase in ρ_{vr} for one-part RuAAC when compared to RuC and two-part RuAAC results available in the literature. This indicates that the mechanism responsible for the drop in f_c is the same for all rubberised materials.
- The elastic modulus, E_c, of one-part RuAAC was significantly lower than that of RuC specimens having the same f_c. Consequently, $\varepsilon_{cr,1}$ of one-part RuAAC was higher than that typically recorded for RuC specimens.
- Constitutive models for the uniaxial compressive stress–strain response and flexural stress-crack width response were presented and validated against the experimental results of this study. The constitutive models, which have been lacking to date, show good agreement with the observed test results.

Future studies can focus on understanding the lower stiffness of one-part RuAAC compared with cement-based counterparts at a micro-structural level. Specific additives such as nanoparticles, other supplementary cementitious materials, or fibres, can then be explored to enhance the stiffness. This would be important to improve the long-term performance of one-part RuAAC under sustained loading and the associated durability ramifications. Investigations could also consider potential structural applications for this type of concrete, utilising its higher ductility and energy dissipation characteristics, to further promote its use as an alternative to conventional concrete. Possible structural applications could be confined members where the reduction in mechanical properties due to rubber addition can be countered with the use of confinement [87–89], whilst providing enhanced ductility and energy dissipation required for members in seismic zones [51,90–92].

CRediT authorship contribution statement

M. Elzeadani: Conceptualization, Investigation, Methodology, Formal analysis, Writing – original draft. **D.V. Bompa:** Conceptualization, Methodology, Writing – review & editing, Supervision. **A.Y. Elghazouli:** Conceptualization, Methodology, Resources, Writing – review & editing, Supervision.

Declaration of Competing Interest

The authors declare that they have no known competing financial interests or personal relationships that could have appeared to influence the work reported in this paper.

Data availability

Data will be made available on request.

Acknowledgements

The first author acknowledges the funding provided by the President's PhD Scholarship at Imperial College London for his research studies. The authors would also like to thank the technical staff at the Structures Laboratory of Imperial College London, particularly Mr. Les Clark and Mr. Bob Hewitt, for their support with the experimental work. The assistance of Dr. Marcus Yio from the Centre for Infrastructure Materials at Imperial College London with regards to material characterisation of aluminosilicate precursors is much appreciated. The support of Hanson and Elkem for providing the blast furnace slag (GGBS) and silica fume (SF) used in this research study is also gratefully acknowledged.

References

[1] T. Suwan, M. Fan, Effect of manufacturing process on the mechanisms and mechanical properties of fly ash-based geopolymer in ambient curing temperature, Mater. Manuf. Process. 32 (2017) 461–467, https://doi.org/10.1080/10426914.2016.1198013.
[2] F. Matalkah, L. Xu, W. Wu, P. Soroushian, Mechanochemical synthesis of one-part alkali aluminosilicate hydraulic cement, Mater. Struct. Constr. 50 (2017) 1–12, https://doi.org/10.1617/s11527-016-0968-4.
[3] B. Nematollahi, J. Sanjayan, F.U.A. Shaikh, Synthesis of heat and ambient cured one-part geopolymer mixes with different grades of sodium silicate, Ceram. Int. 41 (2015) 5696–5704, https://doi.org/10.1016/j.ceramint.2014.12.154.
[4] K.-H. Yang, J.-K. Song, Workability loss and compressive strength development of cementless mortars activated by combination of sodium silicate and sodium hydroxide, J. Mater. Civ. Eng. 21 (2009) 119–127, https://doi.org/10.1061/(asce)0899-1561(2009)21:3(119).
[5] H. Xu, J.S.J. Van Deventer, The geopolymerisation of alumino-silicate minerals, Int. J. Miner. Process. 59 (2000) 247–266, https://doi.org/10.1016/S0301-7516(99)00074-5.
[6] A.F. Abdalqader, F. Jin, A. Al-Tabbaa, Development of greener alkali-activated cement: Utilisation of sodium carbonate for activating slag and fly ash mixtures, J. Clean. Prod. 113 (2016) 66–75, https://doi.org/10.1016/j.jclepro.2015.12.010.
[7] S.Y. Oderji, B. Chen, C. Shakya, M.R. Ahmad, S.F.A. Shah, Influence of superplasticizers and retarders on the workability and strength of one-part alkali-activated fly ash/slag binders cured at room temperature, Constr. Build. Mater. 229 (2019), 116891, https://doi.org/10.1016/j.conbuildmat.2019.116891.
[8] M. Dong, M. Elchalakani, A. Karrech, Development of high strength one-part geopolymer mortar using sodium metasilicate, Constr. Build. Mater. 236 (2020), 117611, https://doi.org/10.1016/j.conbuildmat.2019.117611.
[9] P. Sturm, G.J.G. Gluth, C. Jäger, H.J.H. Brouwers, H.C. Kühne, Sulfuric acid resistance of one-part alkali-activated mortars, Cem. Concr. Res. 109 (2018) 54–63, https://doi.org/10.1016/j.cemconres.2018.04.009.
[10] T. Luukkonen, Z. Abdollahnejad, J. Yliniemi, P. Kinnunen, M. Illikainen, One-part alkali-activated materials: A review, Cem. Concr. Res. 103 (2018) 21–34, https://doi.org/10.1016/j.cemconres.2017.10.001.
[11] E. Adesanya, K. Ohenoja, T. Luukkonen, P. Kinnunen, M. Illikainen, One-part geopolymer cement from slag and pretreated paper sludge, J. Clean. Prod. 185 (2018) 168–175, https://doi.org/10.1016/j.jclepro.2018.03.007.
[12] M. Elzeadani, D.V. Bompa, A.Y. Elghazouli, One part alkali activated materials: A state-of-the-art review, J. Build. Eng. 57 (2022), 104871, https://doi.org/10.1016/j.jobe.2022.104871.
[13] A. Hajimohammadi, J.S.J. van Deventer, Characterisation of One-Part Geopolymer Binders Made from Fly Ash, Waste and Biomass Valorization. 8 (2017) 225–233, https://doi.org/10.1007/s12649-016-9582-5.
[14] B.S. Mohammed, S. Haruna, M.M.A. Wahab, M.S. Liew, A. Haruna, Mechanical and microstructural properties of high calcium fly ash one-part geopolymer cement made with granular activator, Heliyon. 5 (2019) e02255.
[15] S. Guo, C. Ma, G. Long, Y. Xie, Cleaner one-part geopolymer prepared by introducing fly ash sinking spherical beads : Properties and geopolymerization mechanism, J. Clean. Prod. 219 (2019) 686–697, https://doi.org/10.1016/j.jclepro.2019.02.116.

[16] S. Zhou, C. Ma, G. Long, Y. Xie, A novel non-Portland cementitious material : Mechanical properties, durability and characterization, Constr. Build. Mater. 238 (2020), 117671, https://doi.org/10.1016/j.conbuildmat.2019.117671.
[17] P. Perumal, H. Sreenivasan, T. Luukkonen, A.M. Kantola, V. Telkki, P. Kinnunen, M. Illikainen, High strength one-part alkali-activated slag blends designed by particle packing optimization, Constr. Build. Mater. 299 (2021), 124004, https://doi.org/10.1016/j.conbuildmat.2021.124004.
[18] S.F. Ali Shah, B. Chen, M.R. Ahmad, M.A. Haque, Development of Cleaner One-part geopolymer from lithium slag, J. Clean. Prod. 291 (2021) 125241. 10.1016/j.jclepro.2020.125241.
[19] Q. Luo, Y. Wang, S. Hong, F. Xing, B. Dong, Properties and microstructure of lithium-slag-based geopolymer by one- part mixing method, Constr. Build. Mater. 273 (2021), 121723, https://doi.org/10.1016/j.conbuildmat.2020.121723.
[20] A. Peys, H. Rahier, Y. Pontikes, Potassium-rich biomass ashes as activators in metakaolin-based inorganic polymers, Appl. Clay Sci. 119 (2016) 401–409, https://doi.org/10.1016/j.clay.2015.11.003.
[21] A. Hajimohammadi, T. Ngo, P. Mendis, T. Nguyen, A. Kashani, J.S.J. van Deventer, Pore characteristics in one-part mix geopolymers foamed by H2O2: The impact of mix design, Mater. Des. 130 (2017) 381–391, https://doi.org/10.1016/j.matdes.2017.05.084.
[22] N. Ye, J. Yang, S. Liang, Y. Hu, J. Hu, B. Xiao, Q. Huang, Synthesis and strength optimization of one-part geopolymer based on red mud, Constr. Build. Mater. 111 (2016) 317–325, https://doi.org/10.1016/j.conbuildmat.2016.02.099.
[23] X. Ke, S.A. Bernal, N. Ye, J.L. Provis, J. Yang, One-part geopolymers based on thermally treated red Mud/NaOH blends, J. Am. Ceram. Soc. 98 (2015) 5–11, https://doi.org/10.1111/jace.13231.
[24] P. Sturm, G.J.G. Gluth, H.J.H. Brouwers, H.C. Kühne, Synthesizing one-part geopolymers from rice husk ash, Constr. Build. Mater. 124 (2016) 961–966, https://doi.org/10.1016/j.conbuildmat.2016.08.017.
[25] S.F.A. Shah, B. Chen, S.Y. Oderji, M.A. Haque, M.R. Ahmad, Improvement of early strength of fly ash-slag based one-part alkali activated mortar, Constr. Build. Mater. 246 (2020), 118533, https://doi.org/10.1016/j.conbuildmat.2020.118533.
[26] Y.H. Mugahed Amran, M.G. Soto, R. Alyousef, M. El-Zeadani, H. Alabduljabbar, V. Aune, Performance investigation of high-proportion Saudi-fly-ash-based concrete, Results Eng. 6 (2020), https://doi.org/10.1016/j.rineng.2020.100118.
[27] M. Amran, R. Alyousef, H. Alabduljabbar, M. El-Zeadani, Clean production and properties of geopolymer concrete; A review, J. Clean. Prod. 251 (2020), 119679, https://doi.org/10.1016/j.jclepro.2019.119679.
[28] L.Y. Ming, O.W. En, H.C. Yong, M.M.A.B. Abdullah, O.S. Ween, Characteristic of One-Part Geopolymer as Building Materials, in: Sustain. Waste Util. Bricks, Concr. Cem. Mater. Charact. Prop. Performance, Appl., 2021: pp. 97–118.
[29] I. Garcia-Lodeiro, A. Palomo, A. Fernández-Jiménez, An overview of the chemistry of alkali-activated cement-based binders, Woodhead Publishing Limited (2015), https://doi.org/10.1533/9781782422884.1.19.
[30] V. Wong, W. Jervis, B. Fishburn, T. Numata, W. Joe, A. Rawal, C.C. Sorrell, P. Koshy, Long-term strength evolution in ambient-cured solid-activator geopolymer compositions, Minerals. 11 (2021) 1–22, https://doi.org/10.3390/min11020143.
[31] W. Wu, F. Matalkah, P. Soroushian, A. Almalkawi, X. Wang, L. Xu, Influence of admixtures on rheological properties and heat of hydration of alkali aluminosilicate cement, Adv. Cem. Res. 29 (2017) 397–403, https://doi.org/10.1680/jadcr.16.00181.
[32] H.S. Hassan, H.A. Abdel-Gawwad, S.R. Vasquez-Garcia, I. Israde-Alcantara, N. Flores-Ramirez, J.L. Rico, M.S. Mohammed, Cleaner production of one-part white geopolymer cement using pre- treated wood biomass ash and diatomite, J. Clean. Prod. 209 (2019) 1420–1428, https://doi.org/10.1016/j.jclepro.2018.11.137.
[33] S.Y. Oderji, B. Chen, M.R. Ahmad, S.F.A. Shah, Fresh and hardened properties of one-part fly ash-based geopolymer binders cured at room temperature: Effect of slag and alkali activators, J. Clean. Prod. 225 (2019) 1–10, https://doi.org/10.1016/j.jclepro.2019.03.290.
[34] A.T. Almalkawi, A. Balchandra, P. Soroushian, Potential of Using Industrial Wastes for Production of Geopolymer Binder as Green Construction Materials, Constr. Build. Mater. 220 (2019) 516–524, https://doi.org/10.1016/j.conbuildmat.2019.06.054.
[35] T. Wei, H. Zhao, C. Ma, A comparison of water curing and standard curing on one-part alkali- activated fly ash sinking beads and slag : Properties, microstructure and mechanisms, Constr. Build. Mater. 273 (2021), 121715, https://doi.org/10.1016/j.conbuildmat.2020.121715.
[36] O. Wan-en, L. Yun-ming, H. Li-ngee, M. Mustafa, A. Bakri, The Effect of Sodium Carbonate on the Fresh and Hardened Properties of Fly Ash-Based One-Part Geopolymer, IOP Conf. Ser. Mater. Sci. Eng. 864 (2020), https://doi.org/10.1088/1757-899X/864/1/012197.
[37] M.H. Samarakoon, P.G. Ranjith, W. Hui Duan, A. Haque, B.K. Chen, Extensive use of waste glass in one-part alkali-activated materials: Towards sustainable construction practices, Waste Manag. 130 (2021) 1–11, https://doi.org/10.1016/j.wasman.2021.04.060.
[38] C. Ma, B. Zhao, L. Wang, G. Long, Y. Xie, Clean and low-alkalinity one-part geopolymeric cement : Effects of sodium sulfate on microstructure and properties, J. Clean. Prod. 252 (2020), 119279, https://doi.org/10.1016/j.jclepro.2019.119279.
[39] I.K. Jeon, J.S. Ryou, S.H. Jakhrani, H.G. Kim, Effects of light-burnt dolomite incorporation on the setting, strength, and drying shrinkage of one-part alkali-activated slag cement, Materials (Basel). 12 (2019) 1–16, https://doi.org/10.3390/ma12182874.
[40] M. Askarian, Z. Tao, B. Samali, G. Adam, R. Shuaibu, Mix composition and characterisation of one-part geopolymers with different activators, Constr. Build. Mater. 225 (2019) 526–537, https://doi.org/10.1016/j.conbuildmat.2019.07.083.
[41] D. Sood, K.M.A. Hossain, Optimizing Precursors and Reagents for the Development of Alkali-Activated Binders in Ambient Curing Conditions, J. Compos. Sci. 5 (2021).
[42] C. Ma, G. Long, Y. Shi, Y. Xie, Preparation of cleaner one-part geopolymer by investigating different types of commercial sodium metasilicate in China, J. Clean. Prod. 201 (2018) 636–647, https://doi.org/10.1016/j.jclepro.2018.08.060.
[43] S.H. Bong, B. Nematollahi, A. Nazari, M. Xia, J. Sanjayan, Efficiency of different superplasticizers and retarders on properties of "one-part" fly ash-slag blended geopolymers with different activators, Materials (Basel). 12 (2019), https://doi.org/10.3390/ma12203410.
[44] T. Luukkonen, Z. Abdollahnejad, K. Ohenoja, P. Kinnunen, M. Illikainen, Suitability of commercial superplasticizers for one-part alkali-activated blast-furnace slag mortar, J. Sustain. Cem. Mater. 8 (2019) 244–257, https://doi.org/10.1080/21650373.2019.1625827.
[45] Y. Alrefaei, Y.S. Wang, J.G. Dai, The effectiveness of different superplasticizers in ambient cured one-part alkali activated pastes, Cem. Concr. Compos. 97 (2019) 166–174, https://doi.org/10.1016/j.cemconcomp.2018.12.027.
[46] B.S. Thomas, R.C. Gupta, A comprehensive review on the applications of waste tire rubber in cement concrete, Renew. Sustain. Energy Rev. 54 (2016) 1323–1333, https://doi.org/10.1016/j.rser.2015.10.092.
[47] A. Siddika, A. Al, R. Alyousef, Y.H.M. Amran, F. Aslani, H. Alabduljabbar, Properties and utilizations of waste tire rubber in concrete : A review, Constr. Build. Mater. 224 (2019) 711–731, https://doi.org/10.1016/j.conbuildmat.2019.07.108.
[48] D.V. Bompa, A.Y. Elghazouli, B. Xu, P.J. Stafford, A.M. Ruiz-Teran, Experimental assessment and constitutive modelling of rubberised concrete materials, Constr. Build. Mater. 137 (2017) 246–260, https://doi.org/10.1016/j.conbuildmat.2017.01.086.
[49] S. Raffoul, R. Garcia, K. Pilakoutas, M. Guadagnini, N.F. Medina, Optimisation of rubberised concrete with high rubber content: An experimental investigation, Constr. Build. Mater. 124 (2016) 391–404, https://doi.org/10.1016/j.conbuildmat.2016.07.054.
[50] T.M. Pham, W. Chen, A.M. Khan, H. Hao, M. Elchalakani, T.M. Tran, Dynamic compressive properties of lightweight rubberized concrete, Constr. Build. Mater. 238 (2020), 117705, https://doi.org/10.1016/j.conbuildmat.2019.117705.
[51] A.Y. Elghazouli, D.V. Bompa, B. Xu, A.M. Ruiz-Teran, P.J. Stafford, Performance of rubberised reinforced concrete members under cyclic loading, Eng. Struct. 166 (2018) 526–545, https://doi.org/10.1016/j.engstruct.2018.03.090.
[52] D.V. Bompa, A.Y. Elghazouli, Stress–strain response and practical design expressions for FRP-confined recycled tyre rubber concrete, Constr. Build. Mater. 237 (2020), 117633, https://doi.org/10.1016/j.conbuildmat.2019.117633.
[53] S. Raffoul, R. Garcia, D. Escolano-Margarit, M. Guadagnini, I. Hajirasouliha, K. Pilakoutas, Behaviour of unconfined and FRP-confined rubberised concrete in axial compression, Constr. Build. Mater. 147 (2017) 388–397, https://doi.org/10.1016/j.conbuildmat.2017.04.175.
[54] A. Mujdeci, D.V. Bompa, A.Y. Elghazouli, Confinement effects for rubberised concrete in tubular steel cross-sections under combined loading, Arch. Civ. Mech. Eng. 21 (2021), https://doi.org/10.1007/s43452-021-00204-8.
[55] M. Elzeadani, D.V. Bompa, A.Y. Elghazouli, Preparation and properties of rubberised geopolymer concrete: A review, Constr. Build. Mater. 313 (2021), 125504, https://doi.org/10.1016/j.conbuildmat.2021.125504.
[56] A. Wongsa, V. Sata, B. Nematollahi, J. Sanjayan, P. Chindaprasirt, Mechanical and thermal properties of lightweight geopolymer mortar incorporating crumb rubber, J. Clean. Prod. 195 (2018) 1069–1080, https://doi.org/10.1016/j.jclepro.2018.06.003.
[57] M. Dong, M. Elchalakani, A. Karrech, B. Yang, Strength and durability of geopolymer concrete with high volume rubber replacement, Constr. Build. Mater. 274 (2021), 121783, https://doi.org/10.1016/j.conbuildmat.2020.121783.
[58] T.M. Pham, J. Liu, P. Tran, V.L. Pang, F. Shi, W. Chen, H. Hao, T.M. Tran, Dynamic compressive properties of lightweight rubberized geopolymer concrete, Constr. Build. Mater. 265 (2020), 120753, https://doi.org/10.1016/j.conbuildmat.2020.120753.
[59] S. Rajaei, P. Shoaei, M. Shariati, F. Ameri, H.R. Musaeei, B. Behforouz, J. de Brito, Rubberized alkali-activated slag mortar reinforced with polypropylene fibres for application in lightweight thermal insulating materials, Constr. Build. Mater. 270 (2021), 121430, https://doi.org/10.1016/j.conbuildmat.2020.121430.
[60] Y. Park, A. Abolmaali, Y.H. Kim, M. Ghahremannejad, Compressive strength of fly ash-based geopolymer concrete with crumb rubber partially replacing sand, Constr. Build. Mater. 118 (2016) 43–51, https://doi.org/10.1016/j.conbuildmat.2016.05.001.
[61] H. Wang, Y. Wu, B. Cheng, Mechanical properties of alkali-activated concrete containing crumb rubber particles, Case Stud. Constr. Mater. 16 (2022) e00803.
[62] A. Abdelmonim, D.V. Bompa, Mechanical and fresh properties of multi-binder geopolymer mortars incorporating recycled rubber particles, Infrastructures. 6 (2021), https://doi.org/10.3390/infrastructures6100146.
[63] A.M. Aly, M.S. El-Feky, M. Kohail, E.S.A.R. Nasr, Performance of geopolymer concrete containing recycled rubber, Constr. Build. Mater. 207 (2019) 136–144, https://doi.org/10.1016/j.conbuildmat.2019.02.121.
[64] B.S. En, 12350–2:2019, Testing fresh concrete Part 2, Slump test (2019).
[65] BS EN 12390-7, Testing hardened concrete - Part 7: Density of hardened concrete, 2019.

[66] BS EN 12390-3, Testing hardened concrete - Part 3: Compressive strength of test specimens, 2019.
[67] BS EN 12390-6, Testing hardened concrete - Part 6: Tensile splitting strength of test specimens, (2009).
[68] BS EN 12390-5, Testing hardened concrete - Part 5: Flexural strength of test specimens, 2019.
[69] LaVision, Product Manual for 10.2 StrainMaster, 2021. http://www.lavision.de/en/downloads/manuals/systems.php.
[70] LaVision, DaVis digital image correlation software, (n.d.). http://www.lavision.de/en/downloads/software/index.php (accessed December 30, 2021).
[71] N. Singh, P. Kumar, P. Goyal, Reviewing the behaviour of high volume fly ash based self compacting concrete, J. Build. Eng. 26 (2019), 100882, https://doi.org/10.1016/j.jobe.2019.100882.
[72] E. Ahn, H. Kim, S.H. Sim, S.W. Shin, M. Shin, Principles and applications of ultrasonic-based nondestructive methods for self-healing in cementitious materials, Materials (Basel). 10 (2017) 21–25, https://doi.org/10.3390/ma10030278.
[73] N. Ismail, H. El-hassan, Development and Characterization of Fly Ash – Slag Blended Geopolymer Mortar and Lightweight Concrete, J. Mater. Civ. Eng. 30 (2018) 1–14, https://doi.org/10.1061/(ASCE)MT.1943-5533.0002209.
[74] J. Shang, J. Dai, T. Zhao, S. Guo, P. Zhang, B. Mu, Alternation of traditional cement mortars using fly ash-based geopolymer mortars modified by slag, J. Clean. Prod. 203 (2018) 746–756, https://doi.org/10.1016/j.jclepro.2018.08.255.
[75] T. Luukkonen, Z. Abdollahnejad, J. Yliniemi, P. Kinnunen, M. Illikainen, Comparison of alkali and silica sources in one-part alkali-activated blast furnace slag mortar, J. Clean. Prod. 187 (2018) 171–179, https://doi.org/10.1016/j.jclepro.2018.03.202.
[76] L. Coppola, D. Coffetti, E. Crotti, G. Gazzaniga, T. Pastore, The Durability of One-Part Alkali-Activated Slag-Based Mortars in Different Environments, Sustainability. 12 (2020).
[77] A. Wetzel, B. Middendorf, Influence of silica fume on properties of fresh and hardened ultra-high performance concrete based on alkali-activated slag, Cem. Concr. Compos. 100 (2019) 53–59, https://doi.org/10.1016/j.cemconcomp.2019.03.023.
[78] W. Long, H. Li, J. Wei, F. Xing, N. Han, Sustainable use of recycled crumb rubbers in eco-friendly alkali activated slag mortar : Dynamic mechanical properties, J. Clean. Prod. 204 (2018) 1004–1015, https://doi.org/10.1016/j.jclepro.2018.08.306.
[79] BS 8500-1:2015+A2:2019, Complementary British Standard to BS EN 206 - Method of specifying and guidance for the specifier, 2019.
[80] D. Li, Y. Zhuge, R. Gravina, J.E. Mills, Compressive stress strain behavior of crumb rubber concrete (CRC) and application in reinforced CRC slab, Constr. Build. Mater. 166 (2018) 745–759, https://doi.org/10.1016/j.conbuildmat.2018.01.142.
[81] Y.C. Guo, J.H. Zhang, G.M. Chen, Z.H. Xie, Compressive behaviour of concrete structures incorporating recycled concrete aggregates, rubber crumb and reinforced with steel fibre, subjected to elevated temperatures, J. Clean. Prod. 72 (2014) 193–203, https://doi.org/10.1016/j.jclepro.2014.02.036.
[82] F. Aslani, A. Deghani, Z. Asif, Development of Lightweight Rubberized Geopolymer Concrete by Using Polystyrene and Recycled Crumb-Rubber Aggregates, J. Mater. Civ. Eng. 32 (2020) 04019345, https://doi.org/10.1061/(asce)mt.1943-5533.0003008.
[83] M.P. Nielsen, L.C. Hoang, Limit Analysis and Concrete Plasticity, CRC Press, Taylor and Francis Group, Boca Raton, Florida, Third, 2010.
[84] A. Noushini, F. Aslani, A. Castel, R.I. Gilbert, B. Uy, S. Foster, Compressive stress-strain model for low-calcium fly ash-based geopolymer and heat-cured Portland cement concrete, Cem. Concr. Compos. 73 (2016) 136–146, https://doi.org/10.1016/j.cemconcomp.2016.07.004.
[85] T.T. Tran, T.M. Pham, H. Hao, Rectangular Stress-block Parameters for Fly-ash and Slag Based Geopolymer Concrete, Structures. 19 (2019) 143–155, https://doi.org/10.1016/j.istruc.2019.01.006.
[86] D.V. Bompa, B. Xu, A.Y. Elghazouli, Constitutive modelling and mechanical properties of cementitious composites incorporating recycled vinyl banner plastics, Constr. Build. Mater. 275 (2021), https://doi.org/10.1016/j.conbuildmat.2020.122159.
[87] A.P.C. Duarte, B.A. Silva, N. Silvestre, J. de Brito, E. Júlio, J.M. Castro, Tests and design of short steel tubes filled with rubberised concrete, Eng. Struct. 112 (2016) 274–286, https://doi.org/10.1016/j.engstruct.2016.01.018.
[88] M. Elchalakani, M.F. Hassanein, A. Karrech, S. Fawzia, B. Yang, V.I. Patel, Experimental tests and design of rubberised concrete-filled double skin circular tubular short columns, Structures. 15 (2018) 196–210, https://doi.org/10.1016/j.istruc.2018.07.004.
[89] M. Elchalakani, M.F. Hassanein, A. Karrech, B. Yang, Experimental investigation of rubberised concrete-filled double skin square tubular columns under axial compression, Eng. Struct. 171 (2018) 730–746, https://doi.org/10.1016/j.engstruct.2018.05.123.
[90] N. Ganesan, B. Raj, A.P. Shashikala, Behavior of self-consolidating rubberized concrete beam-column joints, ACI Mater. J. 110 (2013) 697–704. 10.14359/51686337.
[91] R. Hassanli, O. Youssf, J.E. Mills, Seismic Performance of Precast Posttensioned Segmental FRP-Confined and Unconfined Crumb Rubber Concrete Columns, J. Compos. Constr. 21 (2017) 1–19, https://doi.org/10.1061/(asce)cc.1943-5614.0000789.
[92] O. Youssf, R. Hassanli, J.E. Mills, X. Ma, Y. Zhuge, Cyclic performance of steel–concrete–steel sandwich beams with rubcrete and LECA concrete core, J. Compos. Sci. 3 (2019), https://doi.org/10.3390/jcs3010005.
[93] N.I. Fattuhi, L.A. Clark, Cement-based materials containing scrap truck tyre rubber, Constr. Build. Mater. 10 (1996) 229–236.
[94] Z.K. Khatib, F.M. Bayomy, Rubberised Portland cement concrete, J. Mater. Civ. Eng. 11 (1999) 206–213.
[95] E. Guneyisi, M. Gesoglu, T. Ozturan, Properties of rubberized concretes containing silica fume, Cem. Concr. Res. 34 (2004) 2309–2317, https://doi.org/10.1016/j.cemconres.2004.04.005.
[96] F. Hernandez-Olivares, G. Barluenga, Fire performance of recycled rubber-filled high-strength concrete, Cem. Concr. Res. 34 (2004) 109–117, https://doi.org/10.1016/S0008-8846(03)00253-9.
[97] A.O. Atahan, U.K. Sevim, Testing and comparison of concrete barriers containing shredded waste tire chips, Mater. Lett. 62 (2008) 3754–3757, https://doi.org/10.1016/j.matlet.2008.04.068.
[98] J. Xue, M. Shinozuka, Rubberized concrete : A green structural material with enhanced energy-dissipation capability, Constr. Build. Mater. 42 (2013) 196–204, https://doi.org/10.1016/j.conbuildmat.2013.01.005.
[99] C. Naito, M. Asce, J. States, C. Jackson, B. Bewick, Assessment of Crumb Rubber Concrete for Flexural Structural Members, J. Mater. Civ. Eng. 26 (2014) 1–8, https://doi.org/10.1061/(ASCE)MT.1943-5533.0000986.
[100] H. Su, J. Yang, T. Ling, G.S. Ghataora, S. Dirar, Properties of concrete prepared with waste tyre rubber particles of uniform and varying sizes, J. Clean. Prod. 91 (2015) 288–296, https://doi.org/10.1016/j.jclepro.2014.12.022.
[101] N.N. Eldin, A.B. Senouci, Rubber-tire particles as concrete aggregate, J. Mater. Civ. Eng. 5 (1993) 478–496.
[102] I.B. Topçu, The properties of rubberized concretes, Cem. Concr. Res. 25 (1995) 304–310, https://doi.org/10.1016/0008-8846(95)00014-3.
[103] R.A. Cairns, H.Y. Kew, M.J. Kenny, in: The Use of Recycled Rubber Tyres in Concrete Construction, Thomas Telford Ltd, London, 2004, pp. 135–142.
[104] A.M. Ghaly, J.D. Cahill IV, Correlation of strength, rubber content, and water to cement ratio in rubberized concrete, Can. J. Civ. Eng. 32 (2005) 1075–1081, https://doi.org/10.1139/L05-063.
[105] M.C. Bignozzi, F. Sandrolini, Tyre rubber waste recycling in self-compacting concrete, Cem. Concr. Res. 36 (2006) 735–739, https://doi.org/10.1016/j.cemconres.2005.12.011.
[106] M.M.R. Taha, A.S. El-Dieb, M.A.A. El-Wahab, M.E. Abdel-Hameed, Mechanical, Fracture, and Microstructural Investigations of rubber concrete, J. Mater. Civ. Eng. 20 (2008) 640–649, https://doi.org/10.1061/(ASCE)0899-1561(2008)20.
[107] M.A. Aiello, F. Leuzzi, Waste tyre rubberized concrete : Properties at fresh and hardened state, Waste Manag. 30 (2010) 1696–1704, https://doi.org/10.1016/j.wasman.2010.02.005.
[108] F. Azevedo, C. Jesus, J.L.B. De Aguiar, A.F. Camões, Properties and durability of HPC with tyre rubber wastes, Constr. Build. Mater. 34 (2012) 186–191, https://doi.org/10.1016/j.conbuildmat.2012.02.062.
[109] F. Liu, W. Zheng, L. Li, W. Feng, G. Ning, Mechanical and fatigue performance of rubber concrete, Constr. Build. Mater. 47 (2013) 711–719, https://doi.org/10.1016/j.conbuildmat.2013.05.055.
[110] H.A. Toutanji, The use of rubber tire particles in concrete to replace mineral aggregates, Cem. Concr. Compos. 18 (1996) 135–139.
[111] F. Hernandez-Olivares, G. Barluenga, M. Bollati, B. Witoszek, Static and dynamic behaviour of recycled tyre rubber-filled concrete, Cem. Concr. Res. 32 (2002) 1587–1596.
[112] A. Turatsinze, M. Garros, On the modulus of elasticity and strain capacity of Self-Compacting Concrete incorporating rubber aggregates, Resour, Conserv. Recycl. 52 (2008) 1209–1215, https://doi.org/10.1016/j.resconrec.2008.06.012.
[113] L. Zheng, X.S. Huo, Y. Yuan, Strength, Modulus of Elasticity, and Brittleness Index of Rubberized Concrete, J. Mater. Civ. Eng. 20 (2008) 692–699, https://doi.org/10.1061/(ASCE)0899-1561(2008)20.
[114] E. Ganjian, M. Khorami, A.A. Maghsoudi, Scrap-tyre-rubber replacement for aggregate and filler in concrete, Constr. Build. Mater. 23 (2009) 1828–1836, https://doi.org/10.1016/j.conbuildmat.2008.09.020.
[115] C. Bing, L. Ning, Experimental Research on Properties of Fresh and Hardened Rubberized Concrete, J. Mater. Civ. Eng. 26 (2014) 1–8, https://doi.org/10.1061/(ASCE)MT.1943-5533.0000923.
[116] A.A. Azmi, M.M.A.B. Abdullah, C.M.R. Ghazali, A. Victor Sandu, K. Hussin, Effect of Crumb Rubber on Compressive Strength of Fly Ash Based Geopolymer Concrete, MATEC Web Conf. 78 (2016) 4–8, https://doi.org/10.1051/matecconf/20167801063.
[117] A.A. Azmi, M.M. Al Bakri, C.M. Ruzaidi, R. Ahmad, L. Musa, L.S. Rou, The Effect of Different Crumb Rubber Loading on the Properties of Fly Ash-Based Geopolymer Concrete, IOP Conf. Ser, Mater. Sci. Eng. 551 (2019), 012079, https://doi.org/10.1088/1757-899X/551/1/012079.
[118] Y. Zaetang, A. Wongsa, P. Chindaprasirt, V. Sata, Utilization of Crumb Rubber As Aggregate in High Calcium Fly Ash Geopolymer Mortars, Int. J. GEOMATE. 17 (2019) 158–165.
[119] I.M. Ali, A.S. Naje, M.S. Nasr, Eco-friendly chopped tire rubber as reinforcements in fly ash based geopolymer concrete, Glob. Nest J. 22 (2020) 342–347. 10.30955/gnj.003192.